metals

MDPI

Article

Effect of Spinel Growth and Texture on Chromium Immobilization During EAF Slag Cooling

Manel Houria [1], Paloma Isabel Gallego [2], Mohammad Jahazi [1] and Elmira Moosavi-Khoonsari [1,*]

[1] Department of Mechanical Engineering, École de Technologie Supérieure, 1100 Notre-Dame St W, Montreal, QC H3C 1K3, Canada; manel.houria@etsmtl.ca (M.H.); mohammad.jahazi@etsmtl.ca (M.J.)
[2] Finkl Steel-Sorel Inc., 100 McCarthy, Sorel-Tracy, QC J3R 3M8, Canada; pgallego@finkl.com
* Correspondence: elmira.moosavi@etsmtl.ca

Abstract

The slag from electric arc furnace (EAF) steelmaking has potential for various applications, but its safe use requires the assessment of heavy metals, such as chromium leaching, to meet environmental standards. This study investigates the microstructure of EAF slag cooled in a slag pot and its effect on Cr immobilization. Slag samples were collected at full scale using a representative sampling method, dividing the slag pot into six zones (internal and external, top to bottom). Microstructural analysis was performed using scanning electron microscopy coupled with energy dispersive spectroscopy and X-ray diffraction, followed by leaching tests on the milled samples. Thermodynamic calculations were performed using FactSage 8.4 to evaluate phase stability and composition. The results indicate that cooling conditions inferred from slag-pot location, spinel size, and spinel zoning are correlated with variations in Cr leaching under neutral conditions. Slower cooling is associated with the formation of large, reverse-zoned spinel phases that may contribute to Cr stabilization, whereas rapid cooling is associated with smaller, homogeneous spinel phases that may increase leaching risk. These findings provide insights for the environmentally safe utilization of EAF slags and inform strategies to minimize Cr release during slag valorization.

Keywords: steelmaking; electric arc furnace slag; chromium leaching; spinel; slag recycling; microstructural characterization

1. Introduction

Electric arc furnace (EAF) steelmaking, mainly scrap-based and operated in mini- and micro-mills, accounts for approximately 31% of global steel production, compared with 69% produced via the blast furnace-basic oxygen furnace (BF–BOF) route, generating roughly 100 kg of slag per ton of liquid steel [1–3]. EAF slag has been widely investigated and applied as a secondary material, notably as a substitute for traditional aggregates in concrete and asphalt, where its angular form enhances mechanical interlocking and strength [4], as well as in road construction for base and sub-base layers and rural driveways [5,6]. In the cement industry, finely ground EAF slag can be blended with clinker to produce Portland slag cement, offering a supplementary cementitious material with reduced environmental impact [7]. Additional applications include landscaping [8], residential gravel alternatives, and erosion control structures [6]. Despite these valorization pathways, approximately 14% of EAF slag is still landfilled worldwide [9].

A major limitation for the widespread and safe utilization of EAF slag is the presence of potentially hazardous elements, particularly chromium. EAF slags can contain up to

Academic Editor: Srecko Stopic

Received: 27 March 2026
Revised: 17 June 2026
Accepted: 18 June 2026
Published: 23 June 2026

2 wt% Cr_2O_3 [4,10], while slags from stainless steel and high-chromium steel production may contain significantly higher levels, typically 6.5 ± 3.8 wt% and occasionally 16 wt% Cr_2O_3. Although chromium is primarily present as immobile and relatively non-toxic Cr^{3+} in fresh slag, long-term environmental exposure and oxidative conditions can promote its oxidation to highly toxic and mobile Cr^{6+}, posing risks to soil and groundwater systems [11–17]. Consequently, most applications require EAF slags to comply with strict environmental regulations, including limits on heavy-metal leachability [18,19]. For example, the U.S. Environmental Protection Agency sets a maximum contaminant level (MCL) of 0.1 mg/L for total chromium in drinking water [20,21], while in Canada, Québec regulations limit chromium leaching from solid waste to 0.5 mg/L [22] (LégisQuébec, accessed 10 September 2025).

Chromium immobilization in EAF slags has therefore been extensively studied, with particular attention to the roles of cooling conditions and temperature [23–30], slag chemistry and basicity [18,28,29,31–33], MgO content [31,34], Al_2O_3 content [28,31,35], FeO content [36], crystallization behavior [18,21,23–25,29–32,34,37,38], and various stabilization strategies [33,34,37,39].

Early work by Tossavainen et al. [23] showed that rapid cooling by water granulation does not necessarily suppress chromium leaching in EAF slags, highlighting the dominant role of phase distribution and glass content. García-Ramos et al. [31] demonstrated that chromium stability depends strongly on MgO and Al_2O_3 availability and slag mineralogy, while Samada et al. [34] showed that mineralogical phase assemblage, rather than Cr_2O_3 concentration, controls chromium dissolution in seawater environments. Cooling rate and thermal history have been identified as key parameters influencing slag phase distribution and chromium partitioning [18,21,25,27,30].

Zhao et al. [24] investigated the effect of cooling from different temperatures on phase transformations, chromium distribution, and the stability of chromium-bearing phases in stainless-steel slag. Their results showed that chromium could be effectively stabilized in spinel during cooling. Li et al. [25] investigated the effect of heating time on the precipitation, composition, and stability of spinel crystals in a synthetic stainless-steel slag. They reported that longer heating promoted spinel crystal growth and increased chromium incorporation, thereby enhancing the chromium stability in the slag. Mombelli et al. [21] aimed to evaluate the effectiveness of two stabilization methods for EAF carbon steel slag to reduce chromium leaching, comparing in-pot and slag-pit treatments. Results showed that in-pot stabilization promoted complete microstructural transformation to a homogeneous gehlenite matrix and coarsened Cr- spinel phases, improving chromium retention. Li and Xue [40] studied the effect of cooling on phase formation and chromium immobilization. They reported that rapid cooling promoted chromium enrichment in the spinel phase, particularly in high-basicity (greater than 2.0) stainless-steel slags. Zeng et al. [27] investigated the crystallization behavior of a synthetic stainless-steel slag. Results showed that spinel is a high-temperature primary phase, an appropriate mineral for the stable curing of chromium, while silicate phases such as β-C_2S, merwinite, and melilite precipitate at lower temperatures. Strandkvist et al. [18] investigated the role of brownmillerite in chromium leaching from low-alloy EAF slags, examining the effect of the cooling rate. Both laboratory and full-scale production confirmed that increasing the cooling rate minimizes the slag brownmillerite content and chromium leaching. Cao et al. [30] studied a controlled cooling method to stabilize chromium in stainless-steel slag from argon–oxygen decarburization (AOD) by promoting the formation of self-wrapped spinel phases. They found that optimal cooling conditions (from around 1300 °C in air) favor chromium enrichment in spinel phases, producing a stable inner–outer spinel structure and minimizing chromium leaching.

The above studies reveal seemingly contradictory effects of cooling. Rapid cooling can suppress the formation of unstable phases such as brownmillerite [18], dicalcium silicate, merwinite, and melilite [24,34], while simultaneously promoting chromium enrichment in spinel [40], improving its immobilization. However, it may also promote the formation of glassy matrices with limited chromium retention [23]. On the other hand, slower cooling and longer holding times generally favor the growth of larger and more crystalline spinel phases [24–26,40], which are often associated with improved chromium stability [21,28,31,36], but can reduce chromium partitioning into spinel [30]. These apparently contradictory observations indicate that chromium immobilization is controlled by a complex interplay between slag chemistry, cooling conditions, and microstructural evolution. Many investigations rely on laboratory-scale or synthetic slags, whereas full-scale slag pots experience highly heterogeneous cooling environments that may strongly influence phase development and chromium stability. The role of spinel texture, size distribution, and compositional zoning, particularly under industrial cooling conditions, also remains insufficiently understood.

In this study, industrial EAF slags subjected to controlled cooling in a slag pot are investigated, with a particular focus on spinel growth, texture, and zoning, and their combined effects on chromium immobilization. Representative full-scale sampling was conducted across different zones of the slag pot to capture cooling heterogeneity. Phase assemblage, phase-specific chromium distribution, and spinel characteristics were characterized using scanning electron microscopy (SEM) coupled with energy-dispersive spectroscopy (EDS) and XRD, followed by standardized leaching tests under neutral and acidic conditions to evaluate total Cr release. The formation of large reverse-zoned spinel phases and their possible role in limiting Cr mobility under industrial cooling conditions were examined to provide practical insights for environmentally responsible slag valorization and improved assessment of EAF slag environmental performance.

2. Methodology

2.1. Experiments

2.1.1. Sample Preparation

After each heat, the EAF slag was poured into a slag pot, which contained up to 1000 kg of sand at the bottom to protect the pot and extend its service life. Each pot could hold the slag from up to four heats, totaling approximately 950 kg. The pot was cooled in place, with the bottom buried for 24 h while the top surface remained exposed to air. Once the slag had fully cooled, samples were collected from six zones within the pot: the internal and external zones at the bottom, middle, and top. The cooling rate was not directly measured but was inferred from the sample location within the slag pot and the expected thermal gradients during cooling. To account for the heterogeneity of the slag, multiple samples were collected from each zone and combined prior to grinding and analysis. Duplicate samples from each zone were prepared for ICP analysis to assess the reproducibility of the observed trends, resulting in a total of 12 analyzed samples. Figure 1 illustrates the sampling locations.

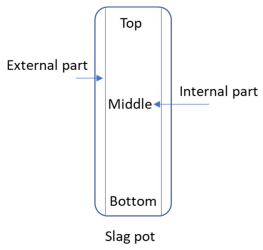

Figure 1. EAF slag sampling scheme from the slag pot.

2.1.2. Microstructural Characterization

The microstructure of the slag samples was analyzed using a Hitachi TM3000 SEM-EDS (Hitachi High-Technologies Corporation, Tokyo, Japan) to determine the composition, phase distribution, particle size, and texture. SEM-EDS analyses were carried out using an accelerating voltage of 15 kV for both imaging and EDS measurements. Analyses were performed in point analysis and elemental mapping modes. For each identified phase, on average, three-point analyses were acquired to obtain representative compositions. The EDS results were treated as semi-quantitative and used primarily for comparative assessment of phase compositions and elemental distributions. Instrument calibration was performed using a pure copper (Cu) standard reference sample, used to adjust both X-ray intensity and peak position accuracy. Representative micrographs were selected based on recurrent and characteristic microstructural features observed across different zones of the slag samples. Spinel particle sizes were measured using the linear intercept method in ImageJ software (version JS) for three SEM micrographs. The average slag composition and binary basicity (B2), which is defined as the mass ratio of CaO to SiO_2 (CaO/SiO_2), are presented in Table 1. The Cr_2O_3 content of the slag was on average 7 ± 4 wt% and could reach up to 16 ± 6 wt%.

Table 1. EAF slag chemical compositions (average values of 16 slag heats).

Slag Chemical Composition (wt% ± σ)							Basicity (B2)	Al_2O_3/SiO_2	FeO/SiO_2
CaO	FeO	SiO_2	Al_2O_3	Cr_2O_3	MnO	MgO			
36 ± 3	25 ± 5	12 ± 3	8 ± 1	7 ± 4	8 ± 2	5 ± 3	3.0	0.67	2.08

XRD analyses were performed using the Malvern Panalytical X'Pert PRO MPD (Malvern Panalytical Ltd., Almelo, The Netherlands) diffractometer between angles $2\theta = 10^\circ$ and 110° with a step size 0.016° and a scan speed of $0.014^\circ/s$, using Co-Kα. The ICDD PDF 4+ 2022 database (manufactured by International Centre for Diffraction Data (ICDD), which is located in Newtown Square, PA, USA) implemented in High Score plus software, which is manufactured by Malvern Panalytical, was used for the qualitative phase identification.

2.1.3. Leaching Tests

Leaching experiments were performed following two Canadian standards: CTEU Method 9 [41] for leaching into water and EPA 1312 for leaching under acid rain conditions [41].

CTEU Method 9:

EAF slag samples were dried at 60 °C and ground to <150 µm. A 2 L round-bottom flask of water containing a few drops of 0.1 N NaOH was prepared to maintain pH 7. Slag samples (40 g) were mixed with 160 mL of leaching solution in HDPE bottles at an L/S ratio of 4:1. Bottles were stirred constantly at 30 rpm for 7 days. After leaching, solutions were filtered through a 0.45 µm filter and analyzed by ICP-OES (Agilent 5110, Agilent Technologies, Santa Clara, CA, USA), with a Cr detection limit of 0.0005 ppm.

EPA 1312:

Slag samples (<9.5 mm) were leached at an L/S ratio of 20:1 (20 g in 400 mL solution). The leaching solution consisted of 950 mL water and 30 mL of a mixed acid solution (14 mL HNO_3 + 16 mL H_2SO_4) to maintain pH 4.20 ± 0.05. Bottles were rotated at 30 rpm for 18 ± 2 h, filtered, and analyzed by ICP-OES. To assess experimental repeatability, duplicate subsamples from each representative slag batch were subjected to independent leaching tests under identical conditions. In addition, each resulting leachate solution was analyzed twice by ICP-OES to evaluate analytical reproducibility.

2.2. Thermodynamic Calculations

Thermodynamic analyses were conducted using FactSage™ 8.4 [42], which is developed by two entities: Thermfact/CRCT in Montreal, Canada, and GTT-Technologies in Herzogenrath, Germany. The effects of equilibrium and non-equilibrium (Scheil) cooling on slag microstructure were investigated. Equilibrium cooling was simulated using the 'Equilib' module, representing extremely slow cooling. Non-equilibrium cooling at higher rates was simulated using the Scheil–Gulliver approach within the same module [43–45]. Slag thermodynamic properties were taken from the FToxid database, and gas-phase properties from FactPS.

3. Results

3.1. Slag Microstructure and Phase Characterization

3.1.1. Phase Assemblage and Chemical Composition (SEM-EDS)

Figures 2 and 3 present the backscattered electron (BSE) images and EDS maps of slag samples collected from the top, middle, and the bottom zones of the internal and external zones, respectively, of the slag pot. The chemical compositions of slag samples collected from different zones of the internal and external zones are presented in Tables 2 and 3 in wt%, respectively. Both internal and external samples mainly contain spinel (Spl), monoxide (MeO) and calcium silicates (Ca-Si). Calcium aluminates (Ca-Al) are predominantly observed in the internal zones, while a Ca-Si-Al phase is identified in the middle-external zone of the slag pot (Table 3).

Table 2. Chemical compositions of slag samples collected from different zones within the internal zone of the slag pot (wt%).

Phase	Mg	Al	Si	Ca	Cr	Mn	Fe	O
Internal top								
Spl	5.46	4.9	2.08	7.91	30.05	4.47	9.92	bal.
std	0.9	1.14	0.33	0.83	2.1	0.67	1.72	
MeO	9.65	1.77	2.3	7.99	1.89	10.46	34.4	bal.
std	0.86	0.57	0.2	0.6	1.13	0.45	1.73	
Ca-Si	0.96	1.38	11.85	37.2	1.61	1.52	5.06	bal.
std	0.12	0.05	0.47	0.49	0.11	0.12	0.38	
Ca-Al	0.30	19.55	1.53	32.76	1.56	1.52	6.72	bal.
std	0.04	0.65	0.87	0.79	0.23	0.06	0.69	
Internal middle								
Spl	5.76	5.88	1.87	6.01	29.36	4.55	9.76	bal.
std	0.46	2.15	0.18	0.71	3.98	0.24	0.40	
MeO	12.13	1.66	2.30	5.93	3.12	10.46	34.56	bal.
std	0.51	0.63	0.74	0.63	0.40	0.57	1.23	
Ca-Si	1.31	6.94	8.91	34.32	2.87	1.29	4.15	bal.
std	0.14	7.77	5.08	3.00	0.30	0.14	0.45	
Ca-Al	1.30	19.52	2.12	28.51	3.34	1.90	6.79	bal.
std	0.41	0.60	1.25	3.51	0.46	0.09	1.33	
Internal bottom								
Spl	6.82	3.87	2.31	6.72	25.90	4.54	11.64	bal.
std	2.41	0.84	0.38	0.29	5.32	0.55	3.25	
MeO	11.42	1.27	2.02	5.98	2.21	9.04	34.00	bal.
std	0.17	0.23	0.54	0.15	0.27	0.50	0.00	
Ca-Si	1.07	1.33	12.43	36.68	2.37	1.19	4.05	bal.
std	0.04	0.25	1.04	1.94	0.49	0.26	0.68	
Ca-Al	0.54	19.24	2.75	32.19	2.17	1.30	5.39	bal.
std	0.26	1.57	0.18	4.33	0.16	0.31	1.47	

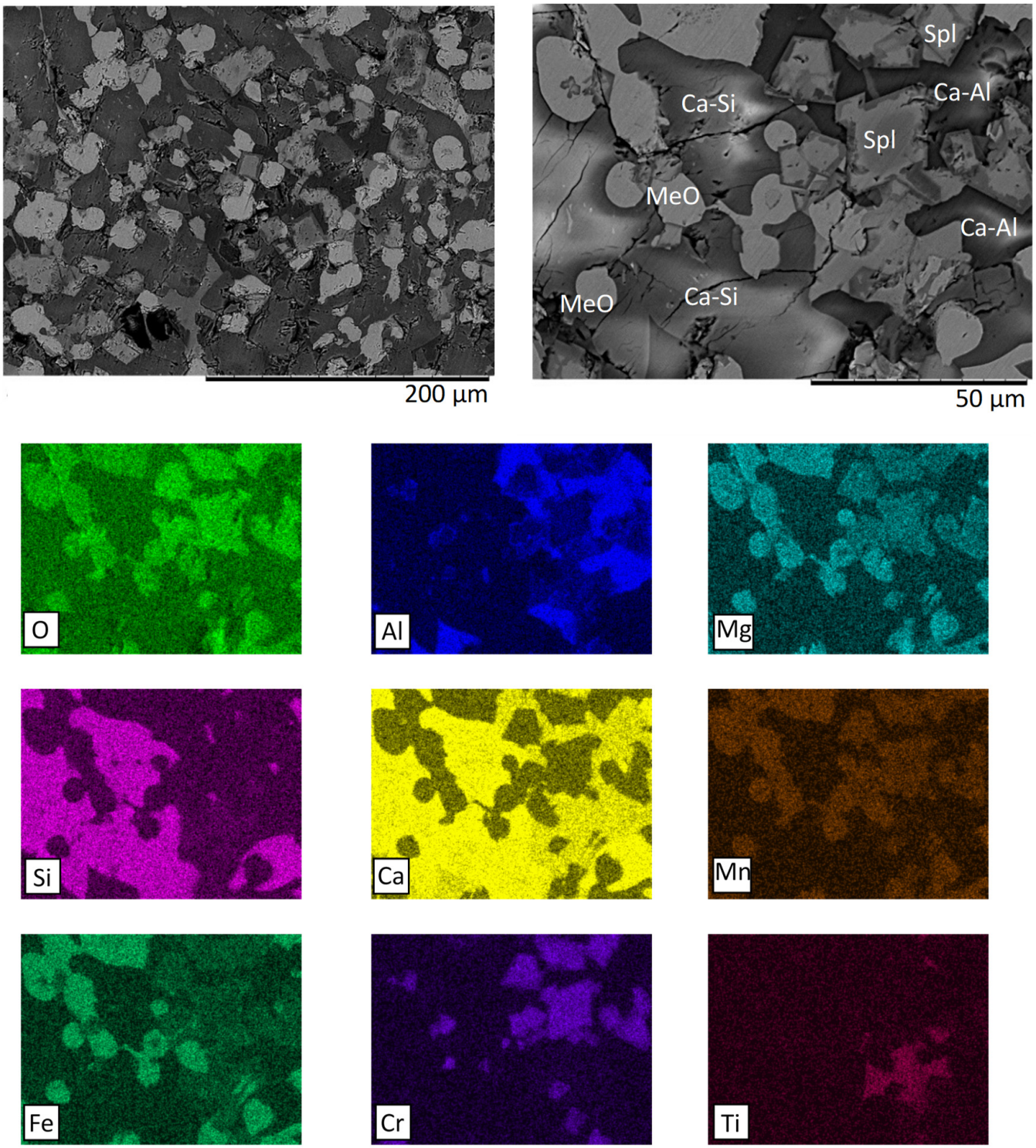

(**a**) internal top

Figure 2. *Cont.*

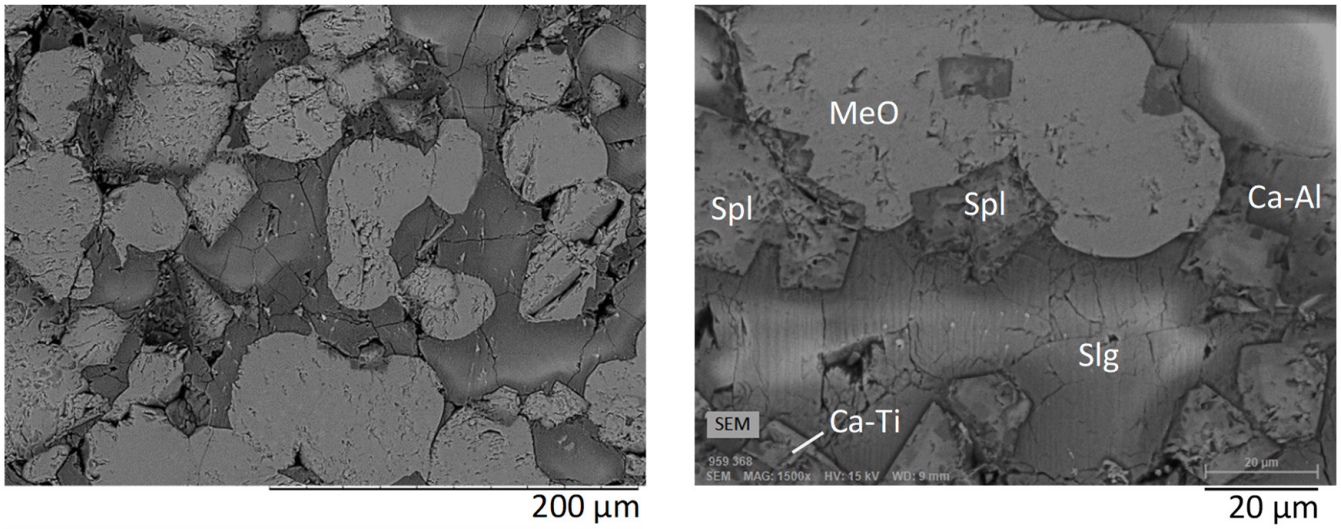

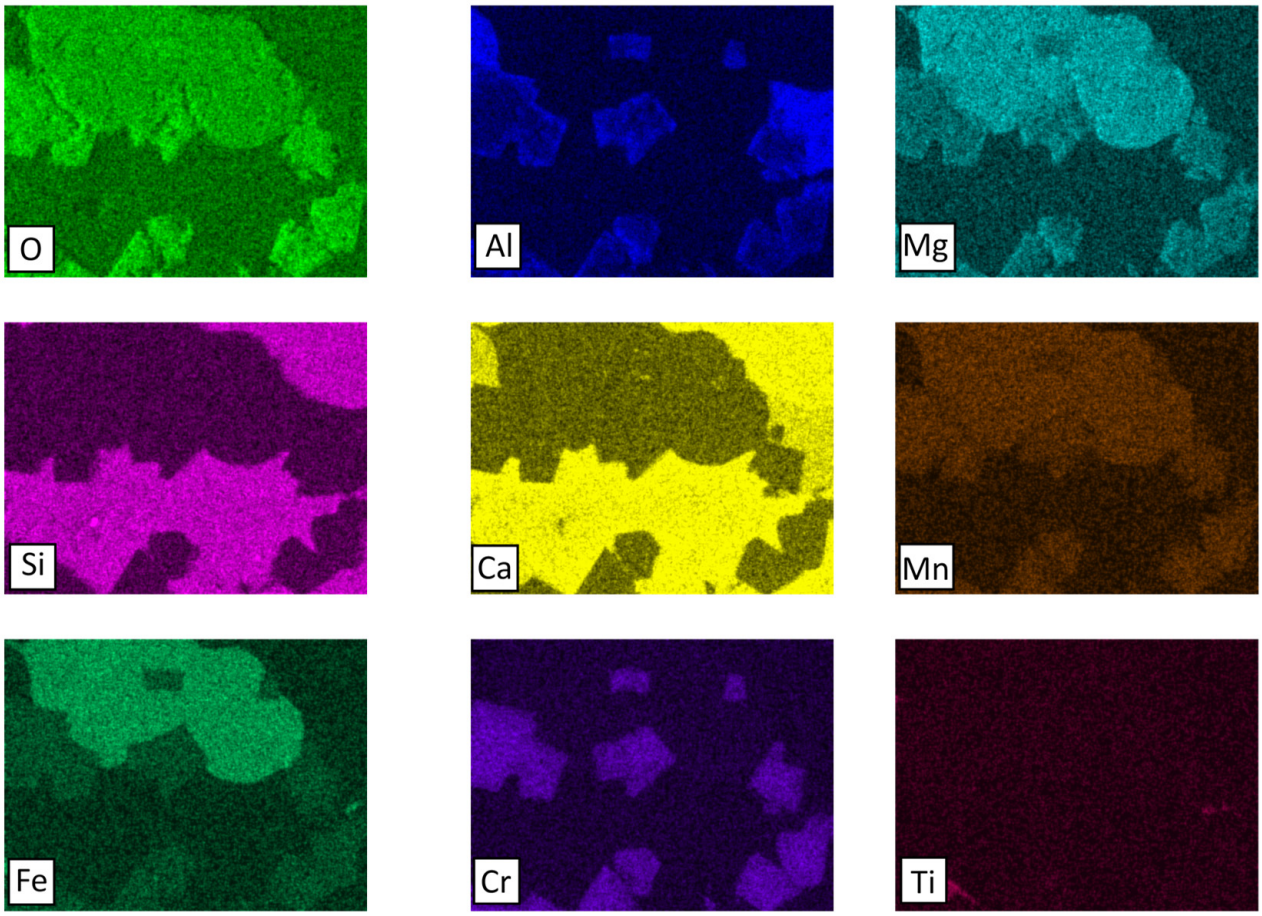

(**b**) Internal middle

Figure 2. *Cont.*

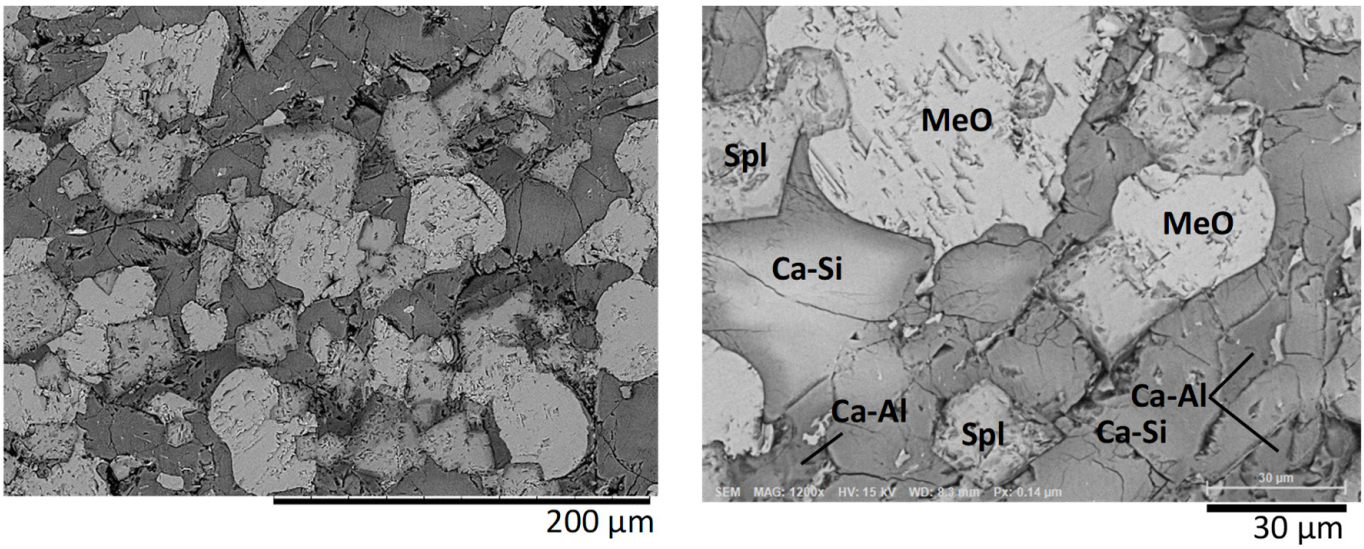

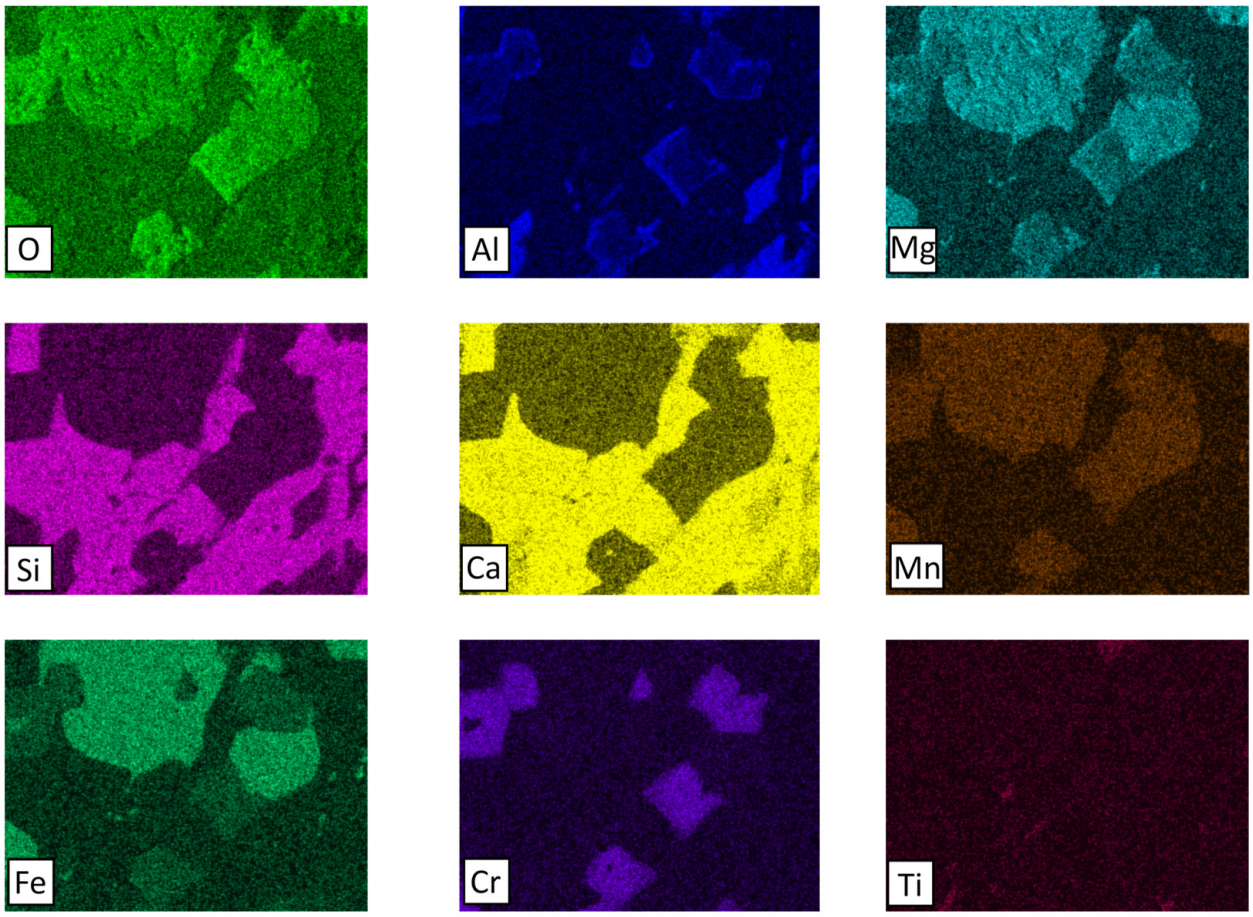

(**c**) internal bottom

Figure 2. BSE images and EDS compositional maps of slag samples from different zones of the internal zone of the slag pot: (**a**) top, (**b**) middle, (**c**) bottom.

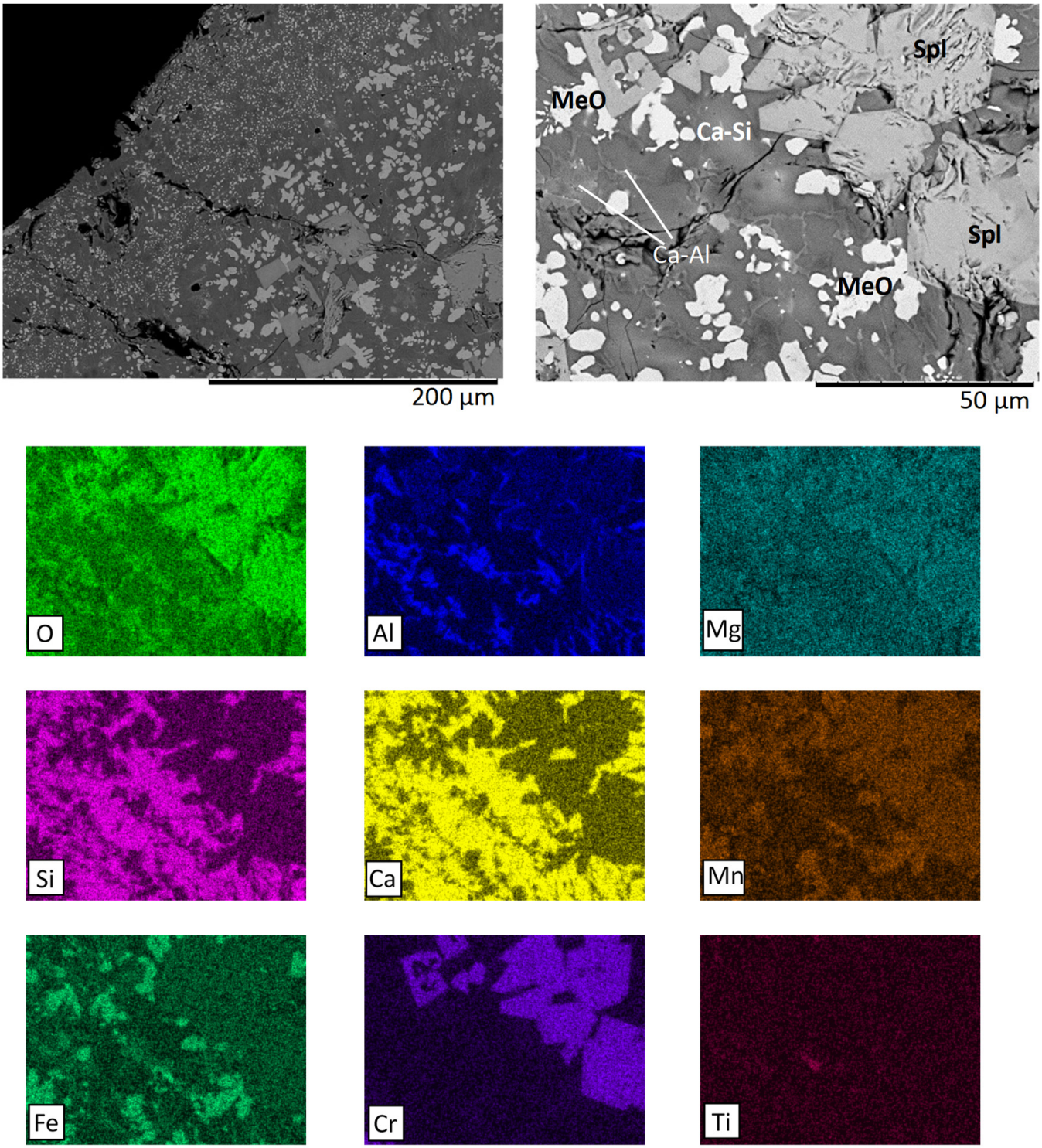

(**a**) External top

Figure 3. *Cont.*

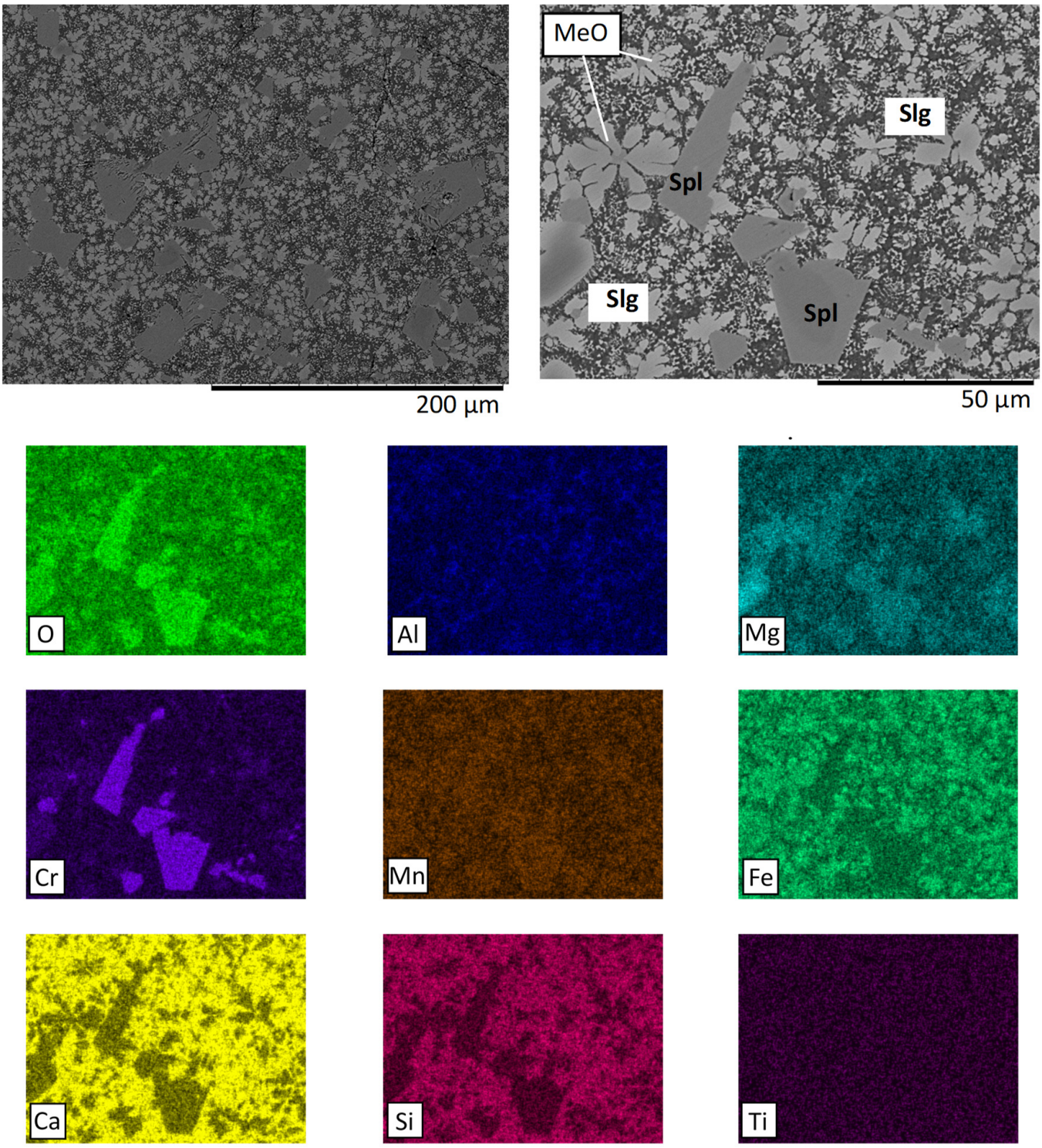

(**b**) External middle

Figure 3. *Cont.*

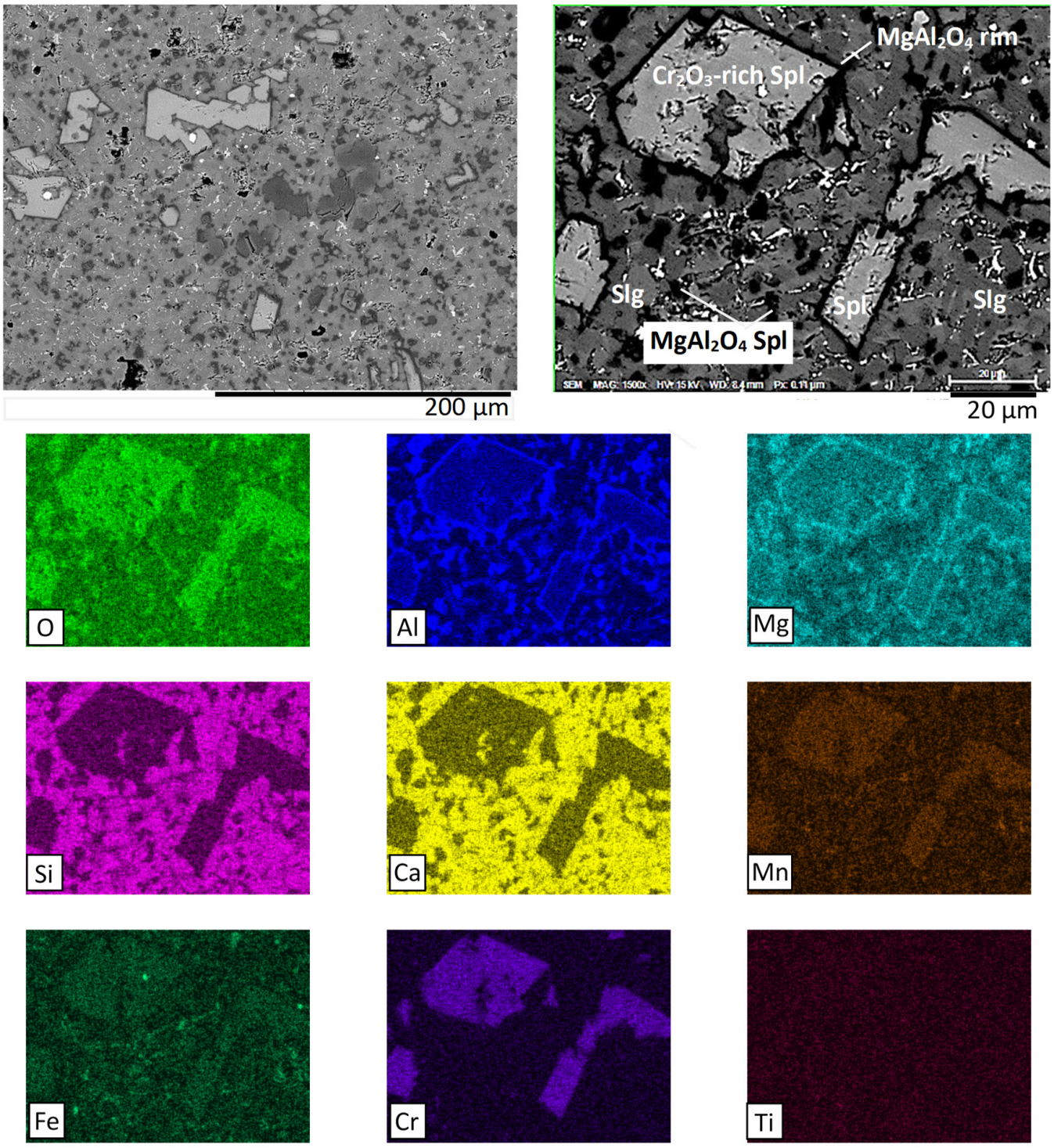

(**c**) External bottom

Figure 3. SEM images and BSE compositional maps of slag samples from different zones of external zone of the slag pot: (**a**) top, (**b**) middle, (**c**) bottom.

Across all analyzed zones, the spinel phase is dominated by Cr, with variable contributions of Fe, Mg, Mn and Ca, and Al. The MeO phase is mainly enriched in Fe, Mn and Mg, with variable contents of Ca and Cr. The Ca-Si phases are characterized by high Ca and Si contents and occasionally contain minor amounts of Cr, Al or Fe. The detailed chemical compositions are presented in the Tables 2 and 3, with each reported composition corresponding to the average of three-point analysis. Titanium was detected locally, partic-

ularly in some Ca-titanate phases observed in the elemental maps; however, it could not be consistently quantified across all phase-specific EDS analyses.

Table 3. Chemical compositions of slag samples collected from different zones within the external zone of the slag pot (wt%).

Phase	Mg	Al	Si	Ca	Cr	Mn	Fe	O
External top								
Spl	4.27	3.01	1.77	4.77	33.09	6.70	8.43	bal.
std	0.31	0.80	0.11	0.29	2.87	0.49	0.38	
MeO	3.90	1.64	2.62	5.78	2.44	15.12	38.06	bal.
std	0.35	0.67	0.09	0.36	0.73	0.56	1.17	
Ca-Si	2.16	4.35	10.50	29.50	1.64	4.93	8.24	bal.
std	0.32	6.00	3.71	10.70	0.18	2.21	5.12	
External middle								
Spl	5.45	1.96	1.57	5.80	34.22	4.36	15.53	bal.
std	0.53	0.63	0.11	0.35	1.60	0.22	0.38	
MeO	7.73	0.89	1.87	7.30	6.64	7.04	40.65	bal.
std	1.06	0.10	0.29	0.90	1.03	0.28	1.44	
Ca-Si	0.70	5.01	8.11	33.54	1.70	2.51	14.91	bal.
std	0.16	0.62	0.98	2.78	0.12	0.59	2.83	
Ca-Si-Al	0.63	10.16	4.80	29.54	2.51	2.70	15.85	bal.
std	0.11	0.82	0.99	2.71	0.90	0.28	2.41	
External bottom								
Spl	6.55	7.65	2.89	6.34	24.52	4.40	6.99	bal.
std	0.07	0.52	0.01	0.14	0.71	0.26	0.53	
Ca-Si	4.44	2.82	13.41	31.83	0.99	2.09	3.15	bal.
std	1.07	0.52	0.20	1.61	0.25	0.39	1.14	

Moreover, compositional variations are observed along the vertical direction of the slag pot, which could be related to variations in the slag composition from different heats. In the external zone, the top and bottom zones (Figure 3a,c) contain a Ca-Al phase with a very small grain size, which could not be analyzed accurately. In addition, the MeO phase is not clearly detected in the bottom zone of the external sample (Figure 3c).

3.1.2. Spinel Particle Size and Textural Characteristics

The spinel particle size was measured in slag samples by analyzing approximately 40 particles from different zones. The size of each particle was determined from SEM images by measuring its major and minor axes. The reported particle size corresponds to the average of these two measurements. Figure 4 illustrates the boxplot diagram of spinel crystal size in different slag-pot zones. Overall, the particles are larger in the internal zone than in the external zone. In the internal zone, the spinel sizes are 34 ± 11, 51 ± 17, and 38 ± 16 μm in the top, middle, and bottom zones, respectively. In contrast, in the external zone, the sizes are 22 ± 11, 17 ± 7, and 15 ± 8 μm in the top, middle, and bottom zones, respectively. This difference may be associated with slower cooling conditions in the internal zones, which are thermally insulated by the surrounding slag bed, compared to the external zones, which are more exposed to air. It should be noted that the interpretation of cooling effects is based on inferred thermal conditions rather than direct cooling-rate measurements. On average, spinel particles in the internal part (≈40.83 μm) are more than twice as large as those in the external zone (≈18.28 μm).

The spinel texture in the slag samples was also analyzed from the internal and external zones, as shown in Figure 5. Compositional gradients are clearly observed from slags sampled from the internal and external-bottom zones of the slag pot. The rims of these spinel phases are enriched in Mg and Al, forming $MgAl_2O_4$-rich margins with Cr_2O_3-depleted compositions relative to their Cr_2O_3-rich cores. Spinel phases from the external-top and -middle zones exhibit more homogeneous compositions, with only minor Al enrichment at the rims of some particles. Additional spinel phases such as $Mg(Al,Fe)O_4$ are detected in the middle and bottom zones.

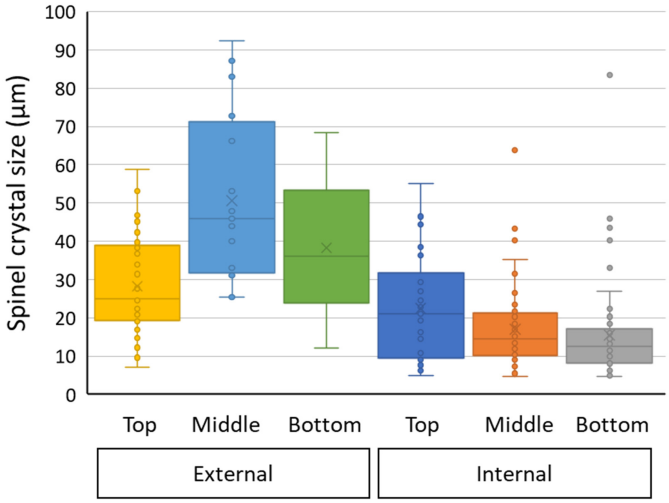

Figure 4. Boxplot diagram of spinel crystal size in different slag-pot zones. Cross symbol represents the mean value.

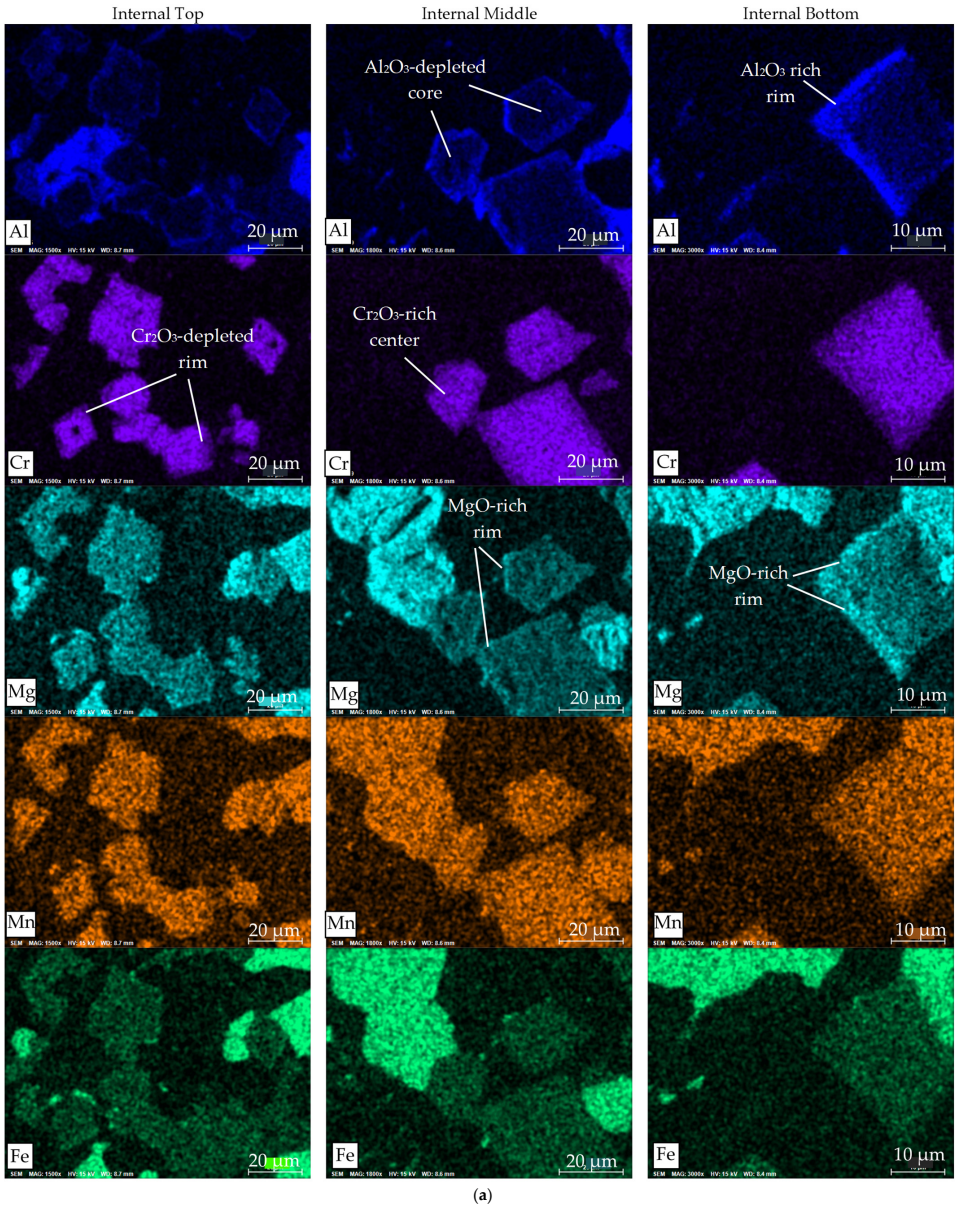

(**a**)

Figure 5. *Cont.*

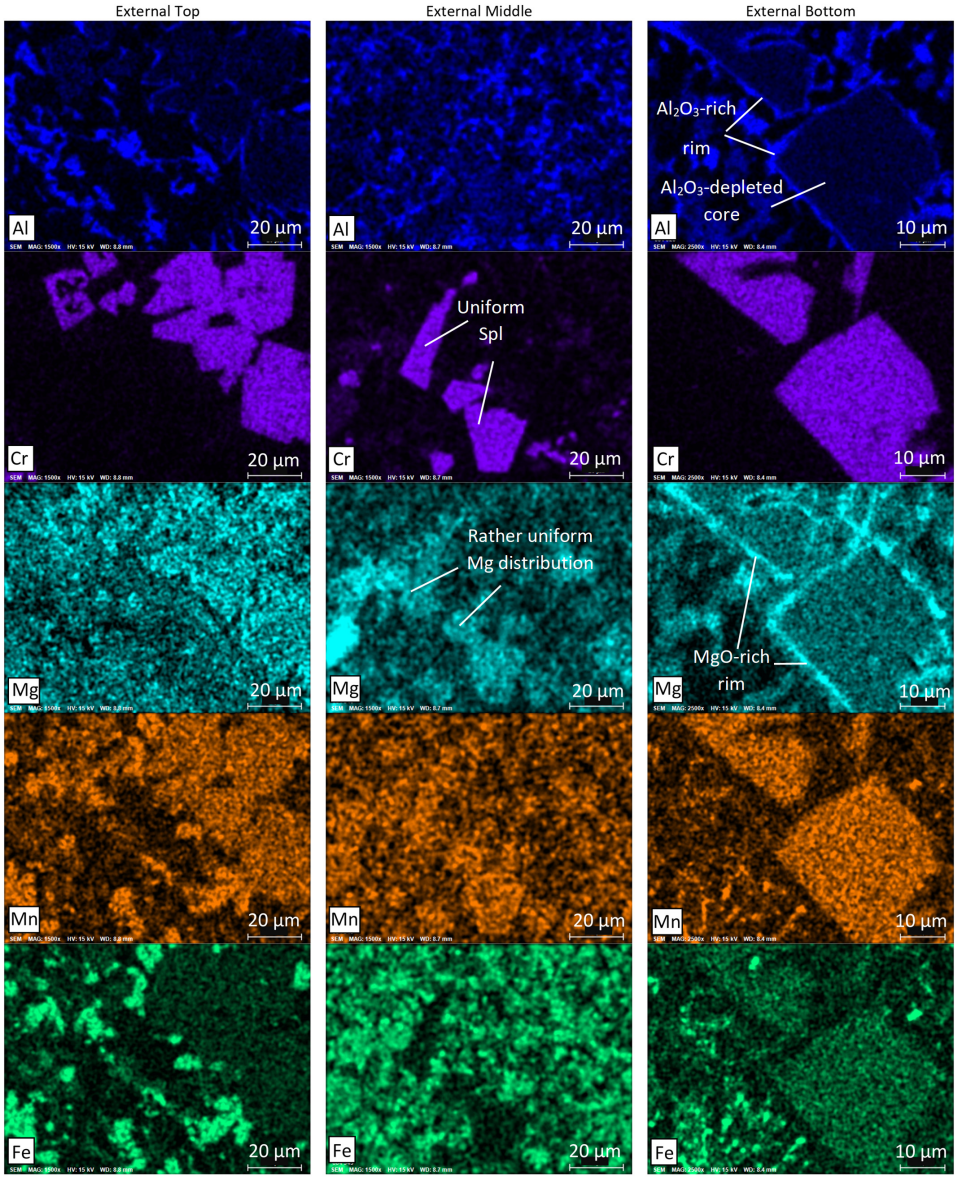

(**b**)

Figure 5. Spinel texture and compositional gradients in slags sampled from different zones of the slag pot: (**a**) internal zone and (**b**) external zone.

3.1.3. Chromium Distribution Among Slag Phases

Chromium concentrations in individual phases (spinel, MeO, and Ca–Si) were quantified for samples from the internal and external zones of the slag pot. Figure 6 shows the distribution of Cr among these phases.

In the external zone, spinel phases show higher Cr contents overall in comparison to the internal zone, with values of ~33–34 wt% in the top and middle zones and a sharp decrease to ~25 wt% at the bottom. The standard deviations in the external zone are within ±1–3 wt%. In the internal zone, spinel Cr content decreases from the top (~30 wt%) to the bottom (~26 wt%), with relatively large standard deviations (±2–5 wt%). This indicates a notable variability in Cr distribution within spinel phases across different depths, mostly due to variations in the slag composition from different heats.

In the external zone, MeO phases exhibit relatively higher Cr contents, particularly in the middle zone (~6.6 wt%), while lower values are observed in the top zone (~2.4 wt%). No measurable Cr content was obtained for the external-bottom zone. In the internal zone,

MeO phases contain low Cr concentrations, ranging from 1.9 to 3.1 wt%, with comparatively moderate standard deviations (±0.3–1.1 wt%).

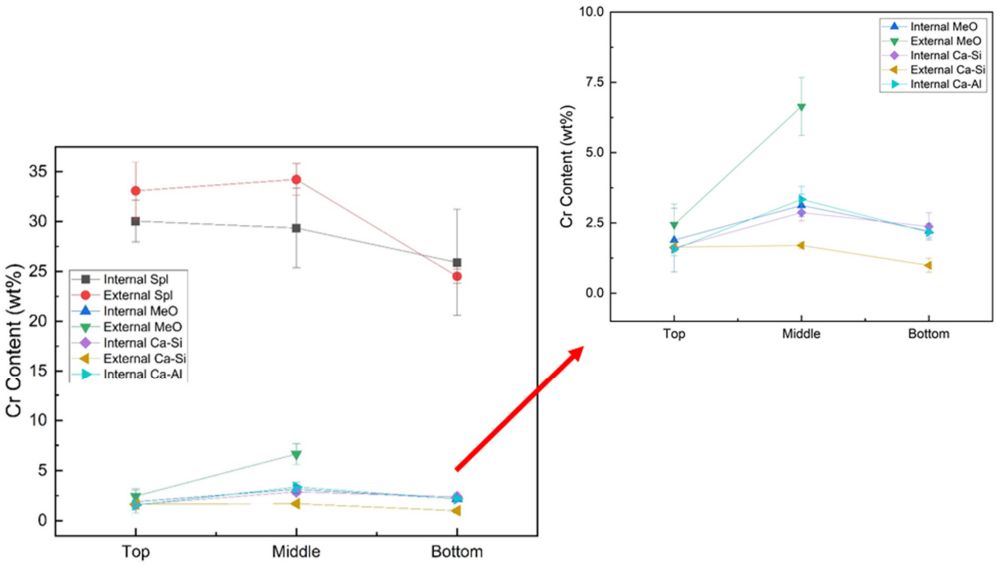

Figure 6. Cr content in different phases of the slag sampled from the internal and external zones, determined using SEM-EDS.

In the external zone, calcium silicates show a relatively great variability, with higher Cr contents in the top zone (~4.9 wt% ± 2.2), no reported values for the middle zone, and lower contents at the bottom (~1.0 wt% ± 0.25). Calcium silicates in the internal zone consistently contain low Cr contents (1.6–2.9 wt%) with very small standard deviations (±0.1–0.5 wt%), indicating limited variability.

3.1.4. Phase Identification by XRD

XRD analyses were conducted on the slag samples to qualitatively identify the major crystalline phases present, complementing the phase compositional and microstructural information obtained from SEM-EDS. The results are presented in Figure 7.

Both internal and external layers consistently contain spinel phases such as $FeCr_2O_4$, $MgCr_2O_4$, and $MnCr_2O_4$ across all zones. Top zones generally have fewer complex spinel phases compared to bottom zones. For example, $Mg(Al,Fe)O_4$ and $(Fe,Mg)Al_2O_4$ spinel phases are mainly found in the bottom zones.

Internal layers often have FeO and MgO as primary MeO phases, whereas external layers lack some MeO phases in the top zone. Calcium silicates (Ca_2SiO_4 or $CaSiO_3$) appear in nearly all layers, indicating that basic silicate formation is consistent throughout. SiO_2 is notable in the lower samples due to the addition of SiO_2 at the bottom of the slag pot to ensure its longevity. Internal layers predominantly contain $Ca_3Al_2O_6$, whereas external layers may contain $CaAl_2O_4$ or mixed alumino-silicates like $Ca_4Al_2Si_2O_{11}$.

$CaTiO_3$ (perovskite) is present in all layers and zones, showing it is stable regardless of position. In addition, no pronounced amorphous hump was observed in the XRD patterns, suggesting that the slags are predominantly crystalline, although the presence of limited amorphous content cannot be excluded.

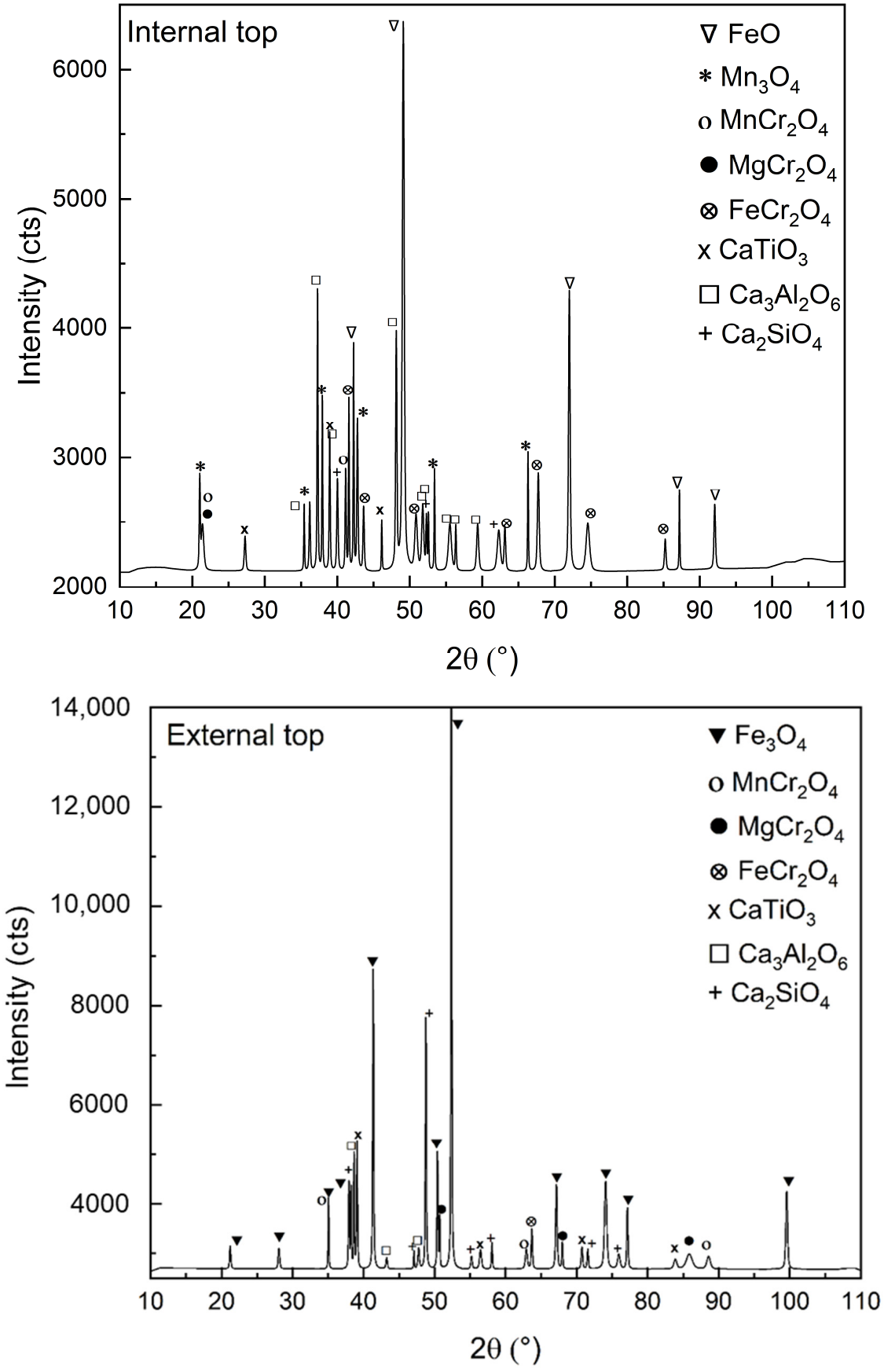

Top zones

Figure 7. *Cont.*

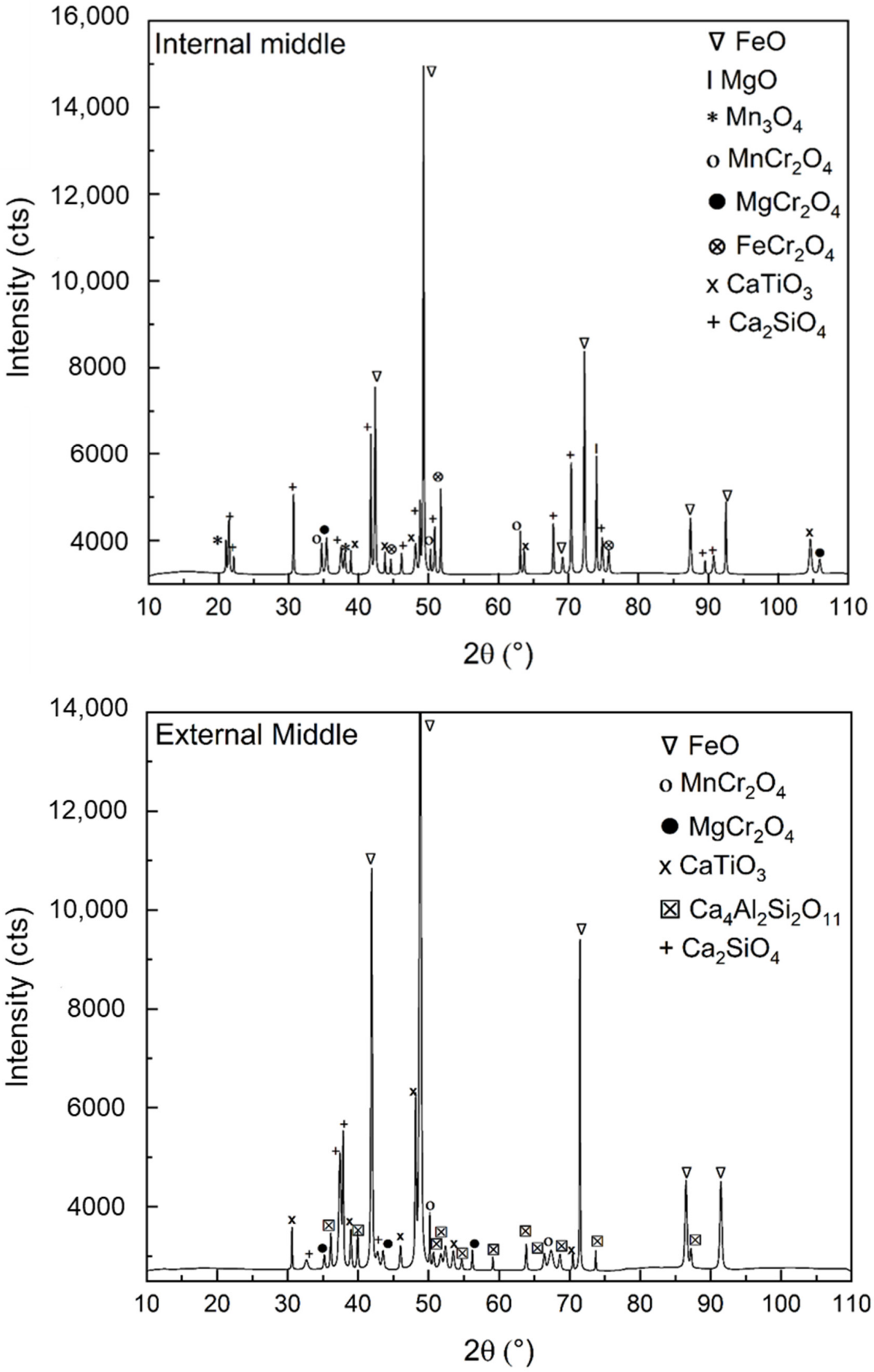

Middle zones

Figure 7. *Cont.*

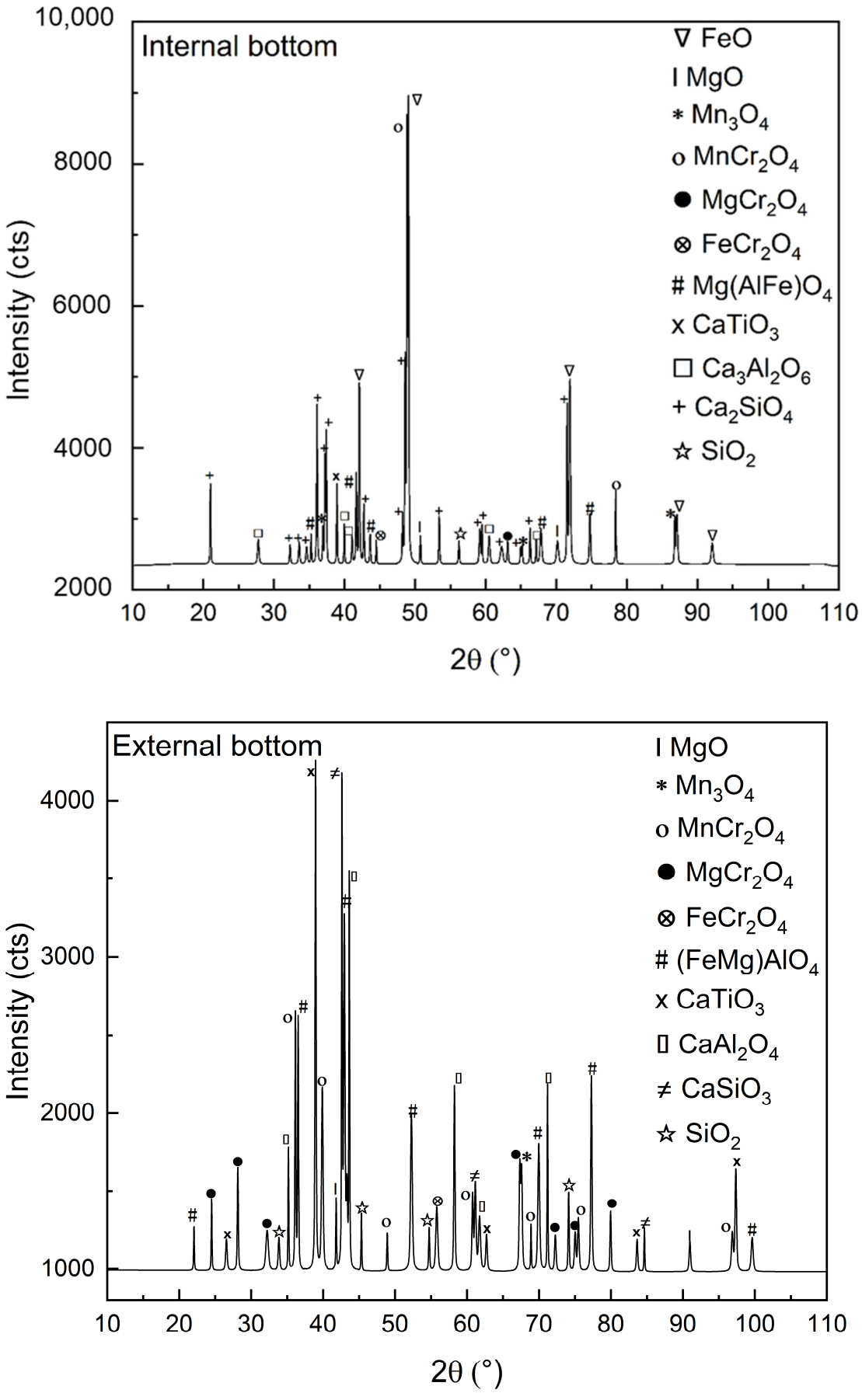

Figure 7. XRD pattern of steel slag.

3.2. Chromium Leaching Behavior

The leaching tests indicate that Cr release varied significantly across zones at neutral pH (7). The internal zone showed very low leaching values (in mg/L), with 0.006 in the top, 0.0025 in the middle, and 0.0225 in the bottom. In contrast, the external zone exhibited much higher leaching values (in mg/L), with 0.0525 in the top, 0.0675 in the middle, and 0.0425 in the bottom, with a standard deviation of 0.0025 ppm. These results demonstrate that leaching was consistently greater in the external zones compared to the internal ones. At acidic conditions (pH = 4.2), the leaching was minimal (below the detection limit of the ICP-OES, i.e., 0.0005 ppm), with only a single measurable value of 0.0025 mg/L for the external bottom zone.

3.3. Calculated Crystallization Path of Slag

The crystallization path of the EAF slag was calculated under both equilibrium and Scheil cooling conditions using FactSage 8.4 databases [42]. Equilibrium cooling assumes complete diffusion in both the liquid and solid phases, corresponding to extremely slow cooling rates, whereas Scheil cooling assumes complete diffusion in the liquid phase only, with no diffusion in the solid. Scheil cooling therefore represents a limiting non-equilibrium condition, intermediate between equilibrium solidification and full quenching, where diffusion is suppressed in both phases. These two approaches were used as bounding cases to qualitatively assess possible phase evolution and Cr partitioning trends during cooling. However, it should be emphasized that these models do not fully reproduce industrial cooling conditions, and the results are constrained by thermodynamic equilibrium assumptions and database limitations, particularly regarding Cr distribution in certain phases. Figure 6 shows the predicted phase distribution, spinel composition, and Cr partitioning among the different phases.

According to the calculations, at the process temperature of 1650 °C, the stable phases are liquid slag (Slg) and tetragonal spinel (TSpl). Approximately 75% of the Cr is predicted to partition into the spinel phase, while the remainder is associated with the liquid slag. Spinel is primarily enriched in Cr, Mn, Al, Fe, and Mg, in decreasing order of concentration. Under very high cooling rates approaching quenching conditions, the calculations suggest that a portion of Cr may remain associated with the residual glassy phase.

Under Scheil cooling conditions (Figure 8a–c), MeO#1 crystallizes first from the slag upon cooling and consists primarily of FeO–MgO with minor MnO. With further cooling, Cr, Mn, and Al contents in the spinel phase increase until saturation at approximately 1119 °C. The MeO phase dissolves only a small fraction of Cr (~1.0 wt%), leading to progressive depletion of Cr in the remaining liquid slag. After complete solidification, the model predicts that most Cr is associated with the spinel phase, while only a minor fraction remains in the MeO phase. Other predicted crystalline phases include bC_2SA (α'-Ca_2SiO_4 solid solution), aC_2SA (α-Ca_2SiO_4 solid solution), and C_2AF. The Ca-silicate phases include Ca_2SiO_4, $FeSi_2O_4$, and Mn_2SiO_4, while C_2AF comprises $Ca_2Al_2O_5$ and $Ca_2Fe_2O_5$. It should be noted that, within the FactSage FToxid database, Cr partitioning is restricted to slag, spinel, and MeO, and is not explicitly considered in Ca-silicate or Ca-aluminate phases, which introduces additional uncertainty into the predicted distribution.

Under equilibrium cooling (Figure 8d–f), spinel remains highly stable, with its Cr content increasing steadily as temperature decreases, while Fe and Mg decline as they partition into other phases. Below approximately 625 °C, all Cr partitions to spinel, with none remaining in MeO. These results indicate that Cr is strongly stabilized in spinel, and its stability increases during cooling. Once incorporated into the spinel structure, Cr becomes effectively fixed and does not redistribute to other phases.

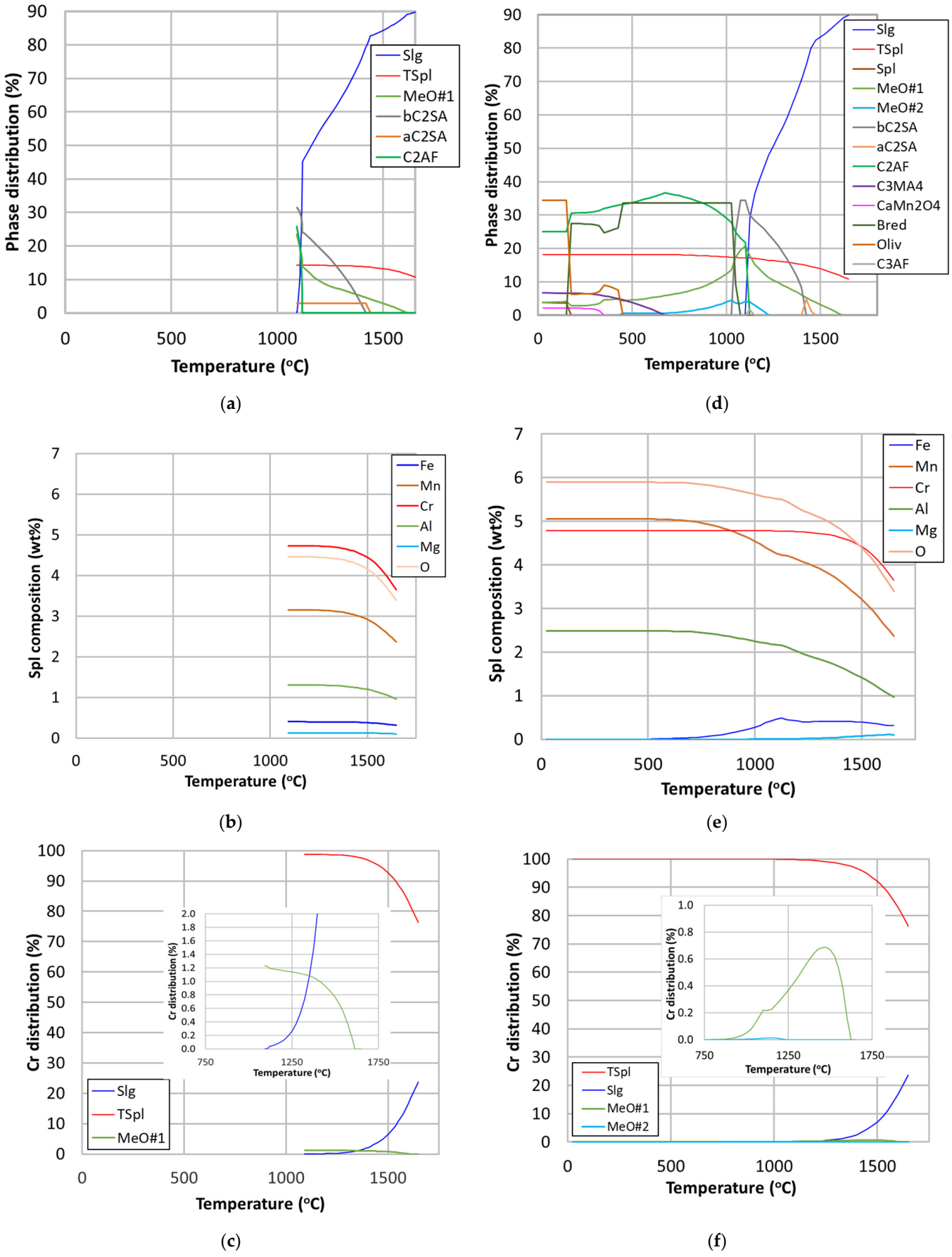

Figure 8. Scheil cooling (**a**–**c**) and equilibrium cooling (**d**–**f**) of EAF slag calculated using FactSage 8.4 databases, showing phase distribution, spinel composition, and Cr phase distribution.

4. Discussion

4.1. Spinel Crystal Size

The leaching results, illustrated in Figure 9, show noticeable differences between the internal and external zones of the slag pot. The internal zones, which are inferred to have experienced slower cooling, developed relatively larger spinel crystals and generally exhibited lower Cr leaching at a neutral pH, whereas the external zones, inferred to have cooled more rapidly, formed finer spinel phases and showed higher leaching levels. This observed trend suggests that the spinel crystal size, which is influenced by cooling conditions, may contribute to differences in Cr release behavior. Within the internal zone, some variation in spinel size is evident, whereas in the external zone, spinel sizes remain relatively similar across zones. It should be noted that since several variables co-vary with slag-pot position, including cooling history and microstructural evolution, this relationship should be interpreted cautiously and does not by itself demonstrate that spinel size is an independent controlling factor for Cr leaching.

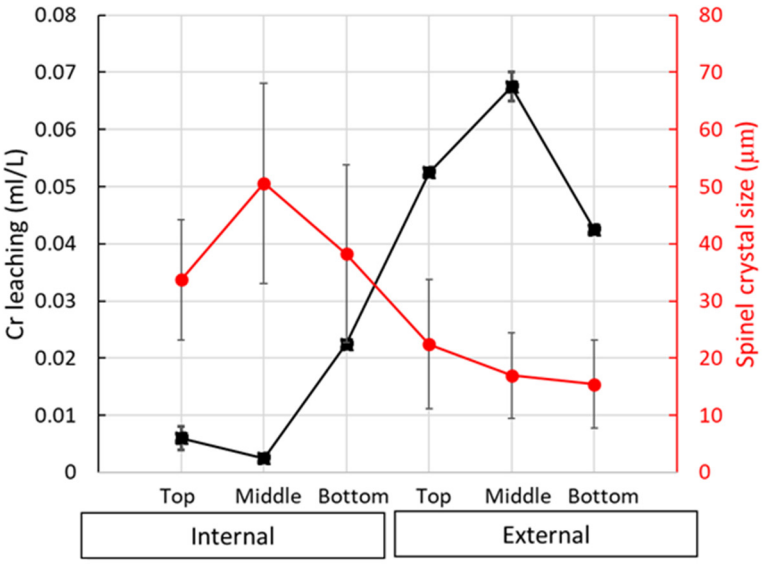

Figure 9. Cr leaching (left axis) and spinel crystal size (right axis) from slags sampled from different zones in the slag pot.

The thermal gradient within the slag pot is likely at the origin of these differences. External zones in contact with the slag-pot wall are inferred to act as primary heat sinks and therefore likely experience more rapid cooling, while internal zones are thermally insulated by the solidified outer shell and are inferred to cool more gradually. These cooling conditions may allow longer diffusion times during solidification in the internal zones, thereby promoting spinel coarsening and microstructural evolution.

These findings are consistent with previous studies reporting that larger spinel phases formed under slower cooling or prolonged heat treatment more effectively immobilize Cr [25,26,28,45]. Conversely, finer spinel particles and smaller fractions are more susceptible to dissolution, increasing Cr release [38]. Kinetic studies indicating surface-reaction-controlled leaching of Fe and Cr are also consistent, further supporting this interpretation [46].

In acidic conditions (pH = 4.2), Cr leaching was nearly negligible regardless of spinel size or cooling history, with only a single measurable value (0.0025 mg/L) detected for the external bottom zone. This shows that, under the specific conditions of the EPA 1312 test, the observed Cr release is very low. Given that multiple experimental parameters differ in this protocol, the combined effects of pH, particle size, liquid-to-solid ratio, and

extraction time likely all contribute to the measured behavior. Nevertheless, within the range of conditions tested, microstructural differences associated with spinel size and cooling history did not appear to significantly influence Cr leaching.

Figure 10 shows a preliminary inverse correlation between average spinel size and Cr leaching at a neutral pH, with a Pearson correlation coefficient of –0.86 (R^2 = 0.74, p = 0.027). Within the examined number of zone-averaged data points, smaller spinel phases were generally associated with higher Cr leaching, and based on the p-value, this correlation is statistically significant.

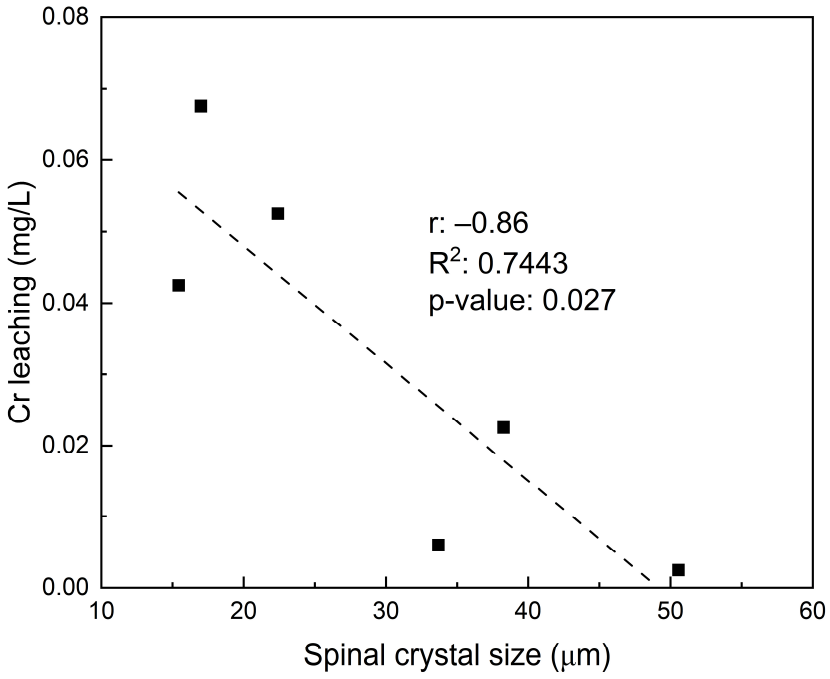

Figure 10. Cr leaching versus spinel crystal size.

While spinel size may contribute to the observed variation in Cr leaching, it does not fully explain the behavior. The remaining variance likely reflects the influence of additional factors, including spinel texture and compositional zoning, as well as contributions from other potentially soluble phases such as calcium silicates and calcium aluminates under neutral conditions.

4.2. Spinel Reverse Zoning

Spinel phases from the internal zones and the external-bottom zone (Figure 5) exhibit pronounced compositional zoning, whereas spinel phases from the external-top and external-middle zones are largely compositionally homogeneous. In the zoned spinel phases, the cores are enriched in Cr and Fe, while the rims are enriched in Mg and Al, forming $MgAl_2O_4$-rich margins with lower Cr_2O_3 contents relative to the core. This reverse zoning is predominantly observed in zones inferred to have experienced slower cooling, likely due to the slag pot's position within the pit and the thermal insulation provided by the surrounding slag layers. However, these thermal conditions are inferred from the spatial position and are not directly measured, and the observed zoning may also reflect combined effects of multiple interacting parameters rather than a single controlling variable. In contrast, external-top and external-middle zones are inferred to have experienced comparatively faster cooling, suggesting limited diffusion and chemical re-equilibration during solidification.

The development of reverse zoning suggests that high-temperature spinel phases formed during slag processing initially crystallized with relatively homogeneous compositions, followed by chemical segregation during comparatively slow cooling. This interpretation is consistent with the XRD results, which show additional spinel phases such as $Mg(Al,Fe)_2O_4$ and $(Mg,Fe)Al_2O_4$ in the bottom zones, reflecting progressive elemental redistribution during cooling.

Previous studies by Zeng et al. [36] and Cao et al. [30] reported normal core–shell spinel phases, characterized by Al- or Mg-rich cores surrounded by Cr-rich rims. In contrast, the present work reveals the formation of reverse-zoned spinel phases, in which Cr- and Fe-rich cores are encapsulated by Mg- and Al-rich rims. Reverse zoning has been attributed to slow cooling, fractional crystallization, reactions with non-homologous melt, or elemental exchange between spinel phases and surrounding silicate phases [47].

This reverse-zoned structure is correlated with enhanced Cr immobilization, particularly in the relatively larger spinel crystals (e.g., ~41 μm) observed in the internal zone. In these spinel phases, Cr appears to be concentrated toward the interior, while the $MgAl_2O_4$-rich rim is hypothesized to potentially reduce direct exposure of Cr-bearing zones to the leaching solution. This suggests a possible diffusion-limiting effect of the Al/Mg-rich rim, which could contribute to kinetically hindered Cr release. However, this interpretation remains a hypothesis based on qualitative microstructural observations, and no independent control of spinel size or zoning was performed, preventing causal attribution.

4.3. Cr Distribution

Spinel is confirmed as the dominant Cr-bearing phase in both internal and external slag zones, containing approximately 25–34 wt% Cr (Figure 5), consistent with the literature identifying spinel as the primary stabilizing phase for chromium in EAF and stainless-steel slags [24,29,31,39,48]. Although external-zone spinel phases are slightly richer in Cr and compositionally more uniform than internal-zone spinel phases, the differences largely overlap within experimental uncertainty, indicating that spinel Cr content alone is not the controlling factor for leaching. This is rather consistent with the observations by Samada et al. [34], who showed that mineralogical phase assemblage, rather than Cr_2O_3 concentration, controls chromium dissolution in seawater environments.

The larger variability in Cr content observed in internal-zone spinel phases likely reflects chemical heterogeneity during slag formation and solidification. Variations in scrap composition during EAF operation can lead to compositional fluctuations along the slag-pot height, which may obscure systematic trends in chemical composition and phase distribution from the top to the bottom of the slag pot. Such variations could have occurred due to cooling gradients and solidification processes.

Previous findings indicate that Mg–wüstite (an MeO phase) can either suppress or enhance Cr leaching depending on composition and stability [21,35]. While Cr contents in internal MeO phases are low, localized enrichment in external-middle samples suggests that MeO can temporarily host Cr depending on local chemistry and cooling history.

Calcium silicates consistently show low Cr contents and greater compositional variability, particularly in the external-top zone, as evidenced in Figures 2, 3 and 6. These phases are widely reported as weak Cr hosts that can contribute to leaching under environmental exposure [24,31,34]. The localized Cr enrichment observed in some external Ca–silicates is heterogeneous and likely unstable, reinforcing their limited role in long-term Cr immobilization.

The weak correlations between Cr leaching and Cr content in individual phases indicate that leaching is largely independent of bulk Cr partitioning among phases. Additionally, despite the high slag basicity (B2 ≈ 3.0), Cr leaching remained very low, particularly

in the internal zones. This is in contrast to Strandkvist et al. (2020) [18], who reported that both decreasing basicity (CaO/SiO_2 ratio) below 2.2 and increasing the rate of cooling could be used to decrease chromium leaching by preventing the formation of brownmillerite.

Overall, these results reveal that cooling history and spinel stability (size and texture) are more critical than Cr concentrations in slag and basicity alone in controlling Cr release.

4.4. Thermodynamic Analysis of Phase Formation

The thermodynamic calculations (Figure 8), particularly Scheil cooling, show reasonable agreement with SEM-EDS (Figures 2 and 3) and XRD data (Figure 7). The thermodynamic calculations (Figure 8), particularly the Scheil cooling simulations, show qualitative consistency with the SEM-EDS observations (Figures 2 and 3) and the XRD phase identification results (Figure 7). These calculations are used here to provide a conceptual framework for understanding possible phase evolution and Cr partitioning trends during cooling, rather than to quantitatively validate the experimental phase assemblages or leaching behavior.

The results suggest that quenching the slag, using methods such as atomization or slag-pit cooling, can trap Cr in the glassy phase, increasing its leaching potential, consistent with Zeng et al. [36] and Strandkvist et al. [18]. They reported that rapid cooling suppresses leachable silicates but can leave Cr in more soluble phases like glass. In contrast, controlled or slow cooling in a slag pot may allow gradual Cr enrichment in spinel, enhancing its stability, in agreement with Mombelli et al. [37] and Cao et al. [30].

Due to the absence of Cr in some phases, such as Ca-silicates and Ca-aluminates, and the lack of Ca in the tetragonal spinel structure, the Cr distribution could be considered approximate. However, the general trend aligns with observations, as Cr solubility in phases other than spinel appears to be low.

At high temperature, the spinel structure can be represented as $(Mn^{2+}, Fe^{2+}, Mg^{2+})(Cr^{3+}, Al^{3+})_2O_4$, with Cr progressively enriching the structure during cooling. Thermodynamic calculations suggest that as spinel crystallizes from the liquid slag, Fe^{2+} and Mg remain relatively constant, while Mn, Al and Cr increase continuously within the spinel structure as growth proceeds. Comparison with the experimentally observed zoning (Figure 5) suggests a possible tendency for Cr enrichment toward the spinel core, whereas Al predominantly concentrates at the rim. This comparison indicates a qualitative agreement between modeled trends and observed zoning patterns rather than a direct mechanistic validation. This behavior is consistent with the reverse zoning observed in spinel phases formed under slow cooling and fractional crystallization conditions from the slag [47], primarily affecting Al and Cr while leaving Mg and Fe^{2+} largely unchanged [49]. However, these interpretations remain qualitative and should be considered within the limitations of the thermodynamic approach used in this study.

5. Conclusions

This study investigated chromium stabilization in EAF slags under spatially variable cooling conditions inferred from the slag-pot location through comparative analysis of samples from different slag-pot zones, examining the correlations between cooling conditions, phase assemblage, spinel microstructure, and Cr leaching. The results suggest that cooling conditions and associated microstructural features, including spinel particle size and texture, can be correlated with variations in Cr stabilization in high-basicity slags, typical of refining operations.

An observed inverse correlation was identified between average spinel crystal size and Cr leaching under neutral conditions. Larger spinel phases formed under inferred slower cooling in the internal zones of the slag pot were generally associated with lower

Cr leaching under neutral conditions. In contrast, smaller spinel phases observed under inferred faster cooling in the external zones were associated with comparatively higher leaching values, although all measured concentrations remained well below the U.S. EPA MCL of 0.1 mg/L. However, the effects of spinel size and zoning, and cooling rate on Cr immobilization during leaching were not independently isolated in this study; therefore, the observed relationships should be interpreted as correlative rather than causal.

Reverse zoning, observed in larger spinel phases, features Cr- and Fe-rich cores surrounded by Mg- and Al-rich rims, which may be associated with reduced accessibility of the leaching environment to the Cr-bearing zones and thereby contribute to lower Cr release. Under relatively rapid cooling conditions, Cr appears to be distributed more homogeneously throughout the spinel structure, which may be associated with the increased accessibility to leaching solutions.

Under acidic conditions tested in this work (pH 4.2), Cr release remained very low across all samples, regardless of spinel size or cooling history. However, since the acidic leaching protocol differs from the neutral test in several experimental parameters, the observed behavior cannot be attributed solely to solution chemistry, and the combined effects of leaching conditions likely contributed to the measured Cr release.

Overall, the results suggest that slower cooling conditions in slag pots are associated with the formation of different spinel microstructures; larger spinel crystals and a reverse zoning texture, in turn, may contribute to improved Cr stabilization. The findings also highlight the importance of representative sampling, as heterogeneous cooling within the slag pot leads to spatial variations in spinel characteristics and corresponding differences in Cr leaching behavior. While further work is required to decouple the effects of cooling history, phase assemblage, and particularly spinel texture—which remains insufficiently investigated—and the present study provides useful insight into the factors that correlated with Cr immobilization under slag-pot cooling conditions. The findings may also contribute to the development of improved practices for slag cooling and handling in steelmaking operations.

Author Contributions: Conceptualization, P.I.G., M.J. and E.M.-K.; methodology, M.H. and E.M.-K.; software, M.H. and E.M.-K.; validation, M.H., P.I.G., M.J. and E.M.-K.; formal analysis, M.H. and E.M.-K.; investigation, M.H. and E.M.-K.; resources, P.I.G., M.J. and E.M.-K.; data curation, M.H.; writing—original draft preparation, M.H. and E.M.-K.; writing—review and editing, M.H., P.I.G., M.J. and E.M.-K.; visualization, M.H. and E.M.-K.; supervision, P.I.G., M.J. and E.M.-K.; project administration, E.M.-K.; funding acquisition, M.J. and E.M.-K. All authors have read and agreed to the published version of the manuscript.

Funding: This research was funded by the Industrial Research Chair in Forming Technologies of High Strength Alloys. The article processing fee (APC) was waived by the journal *Metals*.

Data Availability Statement: The original contributions presented in this study are included in the article. Further inquiries can be directed to the corresponding author.

Acknowledgments: The authors gratefully acknowledge the resources and discussions provided by Finkl Steel-Sorel, as well as Mohammad Saadati, for helping with the XRD characterization, and Kianoosh Kaveh, for assistance with SEM-EDS characterization.

Conflicts of Interest: Author Paloma Isabel Gallego was employed by the company Finkl Steel-Sorel. The remaining authors declare that the research was conducted in the absence of any commercial or financial relationships that could be construed as a potential conflict of interest.

References

1. World Steel Association, Total Production of Crude Steel. Available online: https://worldsteel.org/steel-topics/statistics/annual-production-steel-data/?ind=p1_crude_steel_total_pub/chmn/ind (accessed on 23 October 2023).
2. Kirschen, M.; Hay, T.; Echterhof, T. Process Improvements for Direct Reduced Iron Melting in the Electric Arc Furnace with Emphasis on Slag Operation. *Processes* **2021**, *9*, 402. [CrossRef]
3. Kirschen, M.; Badr, K.; Pfeifer, H. Influence of Direct Reduced Iron on the Energy Balance of the Electric Arc Furnace in Steel Industry. *Energy* **2011**, *36*, 6146–6155. [CrossRef]
4. Teo, P.T.; Zakaria, S.K.; Salleh, S.Z.; Taib, M.A.A.; Mohd Sharif, N.; Abu Seman, A.; Mohamed, J.J.; Yusoff, M.; Yusoff, A.H.; Mohamad, M.; et al. Assessment of Electric Arc Furnace (EAF) Steel Slag Waste's Recycling Options into Value Added Green Products: A Review. *Metals* **2020**, *10*, 1374. [CrossRef]
5. Curry, K.C. Slag—Iron and Steel. In *USGS Minerals Yearbook*; United States Geological Survey: Reston, VA, USA, 2018; pp. 69.1–69.7.
6. Kurecki, M.; Meena, N.; Shyrokykh, T.; Korobeinikov, Y.; Jarnerud Örell, T.; Voss, Z.; Pretorius, E.; Jones, J.; Sridhar, S. Recycling Perspectives of Electric Arc Furnace Slag in the United States: A Review. *Steel Res. Int.* **2025**, *96*, 2300854.
7. Wang, G.C. Slag use in cement manufacture and cementitious applications. In *The Utilization of Slag in Civil Infrastructure Construction*; Elsevier: Oxford, UK, 2016; pp. 305–337.
8. United States Environmental Protection Agency. Electric Arc Furnace (EAF) Slag. Available online: https://www.epa.gov/smm/electic-arc-furnace-eaf-slag (accessed on 23 October 2023).
9. Kim, J.; Azimi, G. Valorization of Electric Arc Furnace Slag via Carbothermic Reduction Followed by Acid Baking—Water Leaching. *Resour. Conserv. Recycl.* **2021**, *173*, 105710. [CrossRef]
10. Wang, G.C. Slag Processing. In *The Utilization of Slag in Civil Infrastructure Construction*; Elsevier: Oxford, UK, 2016; pp. 87–113.
11. Xu, J.; Liu, M.; Ma, G.; Zheng, D.; Zhang, X.; Hou, Y. Valuable Recovery Technology and Resource Utilization of Chromium-Containing Metallurgical Dust and Slag: A Review. *Metals* **2023**, *13*, 1768. [CrossRef]
12. Yang, C.; Zhang, F.; Yu, Y.; Yang, S.; Liu, H.; Wang, H.; Hu, J. An environmentally benign process for effective recovery and solidification of Cr from stainless-steel slag. *J. Clean. Prod.* **2024**, *450*, 141898. [CrossRef]
13. Chaurand, P.; Rose, J.; Briois, V.; Olivi, L.; Hazemann, J.L.; Proux, O.; Domas, J.; Bottero, J.Y. Environmental Impacts of Steel Slag Reused in Road Construction: A Crystallographic and Molecular (XANES) Approach. *J. Hazard. Mater.* **2007**, *139*, 537–542. [CrossRef] [PubMed]
14. Wen, J.; Jiang, T.; Zheng, X.; Wang, J.; Cao, J.; Zhou, M. Efficient Separation of Chromium and Vanadium by Calcification Roasting–Sodium Carbonate Leaching from High Chromium Vanadium Slag and V_2O_5 Preparation. *Sep. Purif. Technol.* **2020**, *230*, 115881. [CrossRef]
15. Lei, D.; Gou, C.; Wang, C.; Xue, J.; Zhang, Z.; Liu, W.; Lin, Z.; Zhang, J. Visible Light Accelerates Cr(III) Release and Oxidation in Cr-Fe Chromite Residues: An Overlooked Risk of Cr(VI) Reoccurrence. *Environ. Sci. Technol.* **2022**, *56*, 17674–17683. [CrossRef] [PubMed]
16. Gurtubay, L.; Gallastegui, G.; Elias, A.; Rojo, N.; Barona, A. Accelerated Ageing of an EAF Black Slag by Carbonation and Percolation for Long-Term Behaviour Assessment. *J. Environ. Manag.* **2014**, *140*, 45–50. [CrossRef]
17. Tan, C.; Liu, H. Inhibition of Hexavalent Chromium Release from Drinking Water Distribution Systems: Effects of Water Chemistry-Based Corrosion Control Strategies. *Environ. Sci. Technol.* **2023**, *57*, 18433–18442. [CrossRef] [PubMed]
18. Strandkvist, I.; Pålsson, K.; Andersson, A.; Olofsson, J.; Lennartsson, A.; Samuelsson, C.; Engström, F. Minimizing Chromium Leaching from Low-Alloy Electric Arc Furnace (EAF) Slag by Adjusting the Basicity and Cooling Rate to Control Brownmillerite Formation. *Appl. Sci.* **2020**, *10*, 35.
19. Cao, L.H.; Liu, C.J.; Zhao, Q.; Jiang, M.F. Analysis on the Stability of Chromium in Mineral Phases in Stainless Steel Slag. *Metall. Res. Technol.* **2018**, *115*, 114.
20. United States Environmental Protection Agency. National Primary Drinking Water Regulations. Available online: https://www.epa.gov/ground-water-and-drinking-water/national-primary-drinking-water-regulations (accessed on 10 September 2025).
21. Mombelli, D.; Barella, S.; Gruttadauria, A.; Mapelli, C.; Le Saout, G.; Garcia-Diaz, E. Effects of Basicity and Mesh on Cr Leaching of EAF Carbon Steel Slag. *Appl. Sci.* **2018**, *9*, 121. [CrossRef]
22. LégisQuébec. Site Officiel de la Législation du Québec. Available online: https://www.legisquebec.gouv.qc.ca/ (accessed on 10 September 2025).
23. Tossavainen, M.; Engstrom, F.; Yang, Q.; Menad, N.; Lidstrom Larsson, M.; Bjorkman, B. Characteristics of Steel Slag under Different Cooling Conditions. *Waste Manag.* **2007**, *27*, 1335–1344. [CrossRef] [PubMed]
24. Zhao, Q.; Liu, C.; Cao, L.; Zheng, X.; Jiang, M. Stability of Chromium in Stainless Steel Slag during Cooling. *Minerals* **2018**, *8*, 445. [CrossRef]

25. Li, J.; Mou, Q.; Zeng, Q.; Yu, Y. Experimental Study on Precipitation Behavior of Spinels in Stainless Steel-Making Slag under Heating Treatment. *Processes* **2019**, *7*, 487. [CrossRef]
26. Huang, W.; Liu, Y. Crystallization Behavior and Growth Mechanisms of Spinel Crystals in Vanadium-Containing Slags. *ISIJ Int.* **2020**, *60*, 2183–2190. [CrossRef]
27. Zeng, Q.; Li, J.; Yu, Y.; Zhu, H. Effect of Cooling Rate on Crystallization Behavior of CaO-SiO_2-MgO-Cr_2O_3 Based Slag. *High Temp. Mater. Process.* **2020**, *39*, 74–80. [CrossRef]
28. Tasnim, T.T. Chromium Stabilization in Ferrochromium Slag for Its Utilization as Aggregate Material. Ph.D. Thesis, The University of British Columbia, Vancouver, BC, Canada, 2021.
29. Cao, S.; Sohn, I.; Wang, Z. Selective Stabilization of Chromium and Sustainable Treatment of Stainless Steel Slags. *J. Environ. Chem. Eng.* **2024**, *12*, 113516. [CrossRef]
30. Cao, S.; Du, C.; Liu, J.; Wei, Y.; Wang, Z. Effective Detoxification of the Cr-Bearing Stainless-Steel Slag by Cooling Control and Self-Wrapped Spinel Precipitation. *J. Environ. Chem. Eng.* **2025**, *13*, 119095. [CrossRef]
31. García-Ramos, E.; Romero-Serrano, A.; Zeifert, B.; Flores-Sanchez, P.; Hallen-Lepez, M.; Palacios, E.G. Immobilization of chromium in slags using MgO and Al_2O_3. *Steel Res. Int.* **2008**, *79*, 332–339. [CrossRef]
32. Li, J.; Zeng, Q.; Mou, Q.; Yu, Y. Effect of Basicity on Precipitation of Spinel Crystals in a CaO-SiO_2-MgO-Cr_2O_3-FeO System. *High Temp. Mater. Process.* **2019**, *38*, 867–872. [CrossRef]
33. Huo, X.; Zhang, X.; Ding, Z.; Zhang, M.; Guo, M. A Clean Approach for Detoxification of Industrial Chromium-Bearing Stainless Steel Slag: Selective Crystallization Control and Binary Basicity Effect. *J. Hazard. Mater.* **2023**, *446*, 130746. [CrossRef] [PubMed]
34. Samada, Y.; Miki, T.; Hino, M. Prevention of Chromium Elution from Stainless Steel Slag into Seawater. *ISIJ Int.* **2011**, *51*, 728–732. [CrossRef]
35. Wang, Z.; Sohn, I. Understanding the Solidification and Leaching Behavior of Synthesized Cr-Containing Stainless Steel Slags with Varying Al_2O_3/SiO_2 Mass Ratios. *Ceram. Int.* **2021**, *47*, 10918–10926. [CrossRef]
36. Zeng, Q.; Li, J.; Mou, Q.; Zhu, H.; Xue, Z. Effect of FeO on Spinel Crystallization and Chromium Stability in Stainless Steel-Making Slag. *JOM* **2019**, *71*, 2331–2337. [CrossRef]
37. Mombelli, D.; Gruttadauria, A.; Barella, S.; Mapelli, C. The Influence of Slag Tapping Method on the Efficiency of Stabilization Treatment of Electric Arc Furnace Carbon Steel Slag (EAF-C). *Minerals* **2019**, *9*, 706. [CrossRef]
38. Mombelli, D.; Dall'Osto, G.; Cozzo, S.; Mapelli, C. Manipulation of the Leaching Behaviour of High-Alloyed Steel EAF Slags through the Particle Size Modulation. *IOP Conf. Ser. Mater. Sci. Eng.* **2024**, *1309*, 012008. [CrossRef]
39. Li, Y.; Gao, J.; Lan, X.; Feng, G.; Zhang, Y.; Guo, Z. An Environmental-Friendly Process for Efficient Recovery of Cr and Harmless Utilization of Stainless Steel Slag via Supergravity. *Sep. Purif. Technol.* **2023**, *310*, 123169. [CrossRef]
40. Li, W.; Xue, X. Effect of Cooling Regime on Phase Transformation and Chromium Enrichment in Stainless-Steel Slag. *Ironmak. Steelmak.* **2018**, *46*, 642–648. [CrossRef]
41. Centre d'Expertise en Analyse Environnementale du Québec. *Normes de lixiviation—MA.100—Lix.Com. 1.1*; Ministère de l'Environnement, de la Lutte Contre les Changements Climatiques: Québec, QC, Canada, 2012; pp. 1–12.
42. Bale, C.W.; Chartrand, P.; Degterov, S.A.; Eriksson, G.; Hack, K.; Mahfoud, R.B.; Melanqon, J.; Pelton, A.D.; Petersen, S. FactSage Thermochemical Software and Databases. *Calphad* **2002**, *26*, 189–228. [CrossRef]
43. Li, Y.; Guo, K.; Xiang, J.; Pei, G.; Lv, X. Effect of Cooling Method on the Mineralogy and Stability of Steel Slag. *ISIJ Int.* **2022**, *62*, 2197–2206. [CrossRef]
44. Kriskova, L.; Pontikes, Y.; Pandelaers, L.; Cizer, Ö.; Jones, P.T.; Van Balen, K.; Blanpain, B. Effect of High Cooling Rates on the Mineralogy and Hydraulic Properties of Stainless Steel Slags. *Metall. Mater. Trans. B Process Metall. Mater. Process. Sci.* **2013**, *44*, 1173–1184. [CrossRef]
45. Albertsson, G.J. Investigations of Stabilization of Cr in Spinel Phase in Chromium-Containing Slags. Licentiate Thesis, KTH Royal Institute of Technology, Stockholm, Sweden, 2011.
46. Zhang, X.; Li, G.; Wu, J.; Xiong, N.; Quan, X. Leaching of Valuable Elements from the Waste Chromite Ore Processing Residue: A Kinetic Analysis. *ACS Omega* **2020**, *5*, 19633–19638. [CrossRef] [PubMed]
47. Bai, Y.; Su, B.X.; Xiao, Y.; Lenaz, D.; Sakyi, P.A.; Liang, Z.; Chen, C.; Yang, S.H. Origin of Reverse Zoned Cr-Spinels from the Paleoproterozoic Yanmenguan Mafic–Ultramafic Complex in the North China Craton. *Minerals* **2018**, *8*, 62. [CrossRef]
48. Cai, S.; Wang, L.; Zhang, Y.; Li, T.; Tian, T.; Liu, T. Transfer and Transformation Mechanism of Chromium in Stainless Steel Slag in Pedosphere. *High Temp. Mater. Process.* **2023**, *42*, 20220252. [CrossRef]
49. Gamal El Dien, H.; Arai, S.; Doucet, L.S.; Li, Z.X.; Kil, Y.; Fougerouse, D.; Reddy, S.M.; Saxey, D.W.; Hamdy, M. Cr-Spinel Records Metasomatism Not Petrogenesis of Mantle Rocks. *Nat. Commun.* **2019**, *10*, 5103. [CrossRef] [PubMed]